

## Snow water equivalent in the Sierra Nevada: Blending snow sensor observations with snowmelt model simulations

Bin Guan,<sup>1,2</sup> Noah P. Molotch,<sup>1,3</sup> Duane E. Waliser,<sup>1</sup> Steven M. Jepsen,<sup>4</sup> Thomas H. Painter,<sup>1</sup> and Jeff Dozier<sup>5</sup>

Received 18 March 2012; revised 10 June 2013; accepted 23 June 2013; published 19 August 2013.

[1] We estimate the spatial distribution of daily melt-season snow water equivalent (SWE) over the Sierra Nevada for March to August, 2000–2012, by two methods: reconstruction by combining remotely sensed snow cover images with a spatially distributed snowmelt model and a blended method in which the reconstruction is combined with in situ snow sensor observations. We validate the methods with 17 snow surveys at six locations with spatial sampling and with the operational snow sensor network. We also compare the methods with NOAA's operational Snow Data Assimilation System (SNODAS). Mean biases of the methods compared to the snow surveys are  $-0.193$  m (reconstruction),  $0.001$  m (blended), and  $-0.181$  m (SNODAS). Corresponding root-mean-square errors are  $0.252$ ,  $0.205$ , and  $0.254$  m. Comparison between blended and snow sensor SWE suggests that the current sensor network inadequately represents SWE in the Sierra Nevada because of the low spatial density of sensors in the lower/higher elevations. Mean correlation with streamflow in 19 Sierra Nevada watersheds is better with reconstructed SWE ( $r = 0.91$ ) versus blended SWE ( $r = 0.81$ ), snow sensor SWE ( $r = 0.85$ ), and SNODAS SWE ( $r = 0.86$ ). On the other hand, the correlation with blended SWE is generally better than with reconstructed, snow sensor, and SNODAS SWE late in the snowmelt season when snow sensors report zero SWE but snow remains in the higher elevations. Sensitivity tests indicate downwelling longwave radiation, snow albedo, forest density, and turbulent fluxes are potentially important sources of errors/uncertainties in reconstructed SWE, and domain-mean blended SWE is relatively insensitive to the number of snow sensors blended.

**Citation:** Guan, B., N. P. Molotch, D. E. Waliser, S. M. Jepsen, T. H. Painter, and J. Dozier (2013), Snow water equivalent in the Sierra Nevada: Blending snow sensor observations with snowmelt model simulations, *Water Resour. Res.*, 49, 5029–5046, doi:10.1002/wrcr.20387.

### 1. Introduction

[2] Understanding mountain hydrological processes is crucial to projections of water supply in California's Sierra Nevada and throughout the western United States, where the seasonal snowpack provides the main source of water for agriculture, recreation, hydropower, urban supply, and downstream habitats [Bales *et al.*, 2006]. Characteristic of Mediterranean climates, the Sierra Nevada's wet winter months (November to March) account for 70–80% of the total annual precipitation [Pandey *et al.*, 1999]. Snow accumulation during the wet season becomes an important

water resource during the dry summer. The distinct snow accumulation and ablation seasons throughout the Sierra Nevada are attributable to regional-scale weather systems, with the mountains enhancing precipitation as they block and lift the moist air [Alpert, 1986; Barros and Lettenmaier, 1994].

[3] Accurate estimates of snow water equivalent (SWE) in mountainous regions are needed for improved hydrological modeling and water resource management [Rice *et al.*, 2011]. Such estimates can also improve regional climate model evaluation [Caldwell *et al.*, 2009] and therefore lead to more robust estimates of hydrological response to regional climate change. Such information will also be helpful in understanding snowmelt-related groundwater dynamics in alpine ecosystems [Lowry *et al.*, 2010]. The complex topography in mountainous regions makes it difficult to interpolate spatially sparse in situ snow observations over large areas [Molotch and Bales, 2005, 2006]. Several studies have documented the topographic controls on snow distribution at the headwater catchment scale, based on densely distributed snow measurements [e.g., Elder *et al.*, 1991; Winstral *et al.*, 2002; Erickson *et al.*, 2005; Molotch *et al.*, 2005a, 2005b], but over large areas such as the whole Sierra Nevada the density of automated snow sensors is about 1 in 700 km<sup>2</sup>. Hence, relationships between observed SWE and physiographic variables are not adequate for robust interpolation or extrapolation over such large regions.

<sup>1</sup>Jet Propulsion Laboratory, California Institute of Technology, Pasadena, California, USA.

<sup>2</sup>Joint Institute for Regional Earth System Science and Engineering, University of California, Los Angeles, California, USA.

<sup>3</sup>Department of Geography and Institute for Arctic and Alpine Research, University of Colorado Boulder, Boulder, Colorado, USA.

<sup>4</sup>Sierra Nevada Research Institute, University of California, Merced, California, USA.

<sup>5</sup>Bren School of Environmental Science and Management, University of California, Santa Barbara, California, USA.

Corresponding author: B. Guan, Jet Propulsion Laboratory, California Institute of Technology, M/S 233–300, 4800 Oak Grove Drive, Pasadena, CA 91109, USA. (bin.guan@jpl.nasa.gov)

[4] Direct estimation of SWE using passive microwave remote sensing has limited utility in the mountains, because subpixel variability in land surface states complicates relationships between SWE and brightness temperature. Active microwave remote sensing has shown promise for SWE measurement at fine spatial resolution [Shi, 2008], but there is no current operational mission for such applications. Airborne remote sensing of SWE via observations of the attenuation of terrain-emitted gamma radiation is regularly conducted throughout the United States by the National Weather Service. However, it is limited to terrain of moderate complexity and to areas with SWE less than about 250 mm [Peck et al., 1971; Carroll et al., 2001]. Mean April 1 SWE in the Sierra Nevada is above 250 mm during most years [Guan et al., 2010], making the technique largely impractical except during anomalously low snow years, at lower elevations, or late in the melt season.

[5] Previous studies have illustrated that snow cover depletion patterns repeat from year to year with the timing of ablation largely controlled by accumulation magnitude [Déry et al., 2005; Sturm and Wagner, 2010]. Methods to reconstruct spatio-temporal variation of SWE combine the satellite-observed rate of snow depletion with a calculation of the melt rate to retroactively estimate, as the snow melts, how much had existed earlier in the season [Martinez and Rango, 1981]. Under the assumption of insignificant ablation-season snow accumulation, such methods can calculate peak SWE by back-integrating the total snowmelt from the time of snow disappearance to the time at which snowmelt begins. Compared to forward modeling, such methods do not rely on accurate estimate of initial SWE nor do they depend on availability of precipitation forcings. In comparison with forward-modeling approaches, the reconstruction approach shows promise for characterizing snow distribution in unsampled regions where forward-modeling approaches are most uncertain [Raleigh and Lundquist, 2012]. In small drainage basins ( $<100 \text{ km}^2$ ) in the western United States, this reconstruction approach has had reasonable success [Cline et al., 1998; Molotch et al., 2004]. Extension of the reconstruction approach to the larger Merced and Tuolumne River basins, California (1403 and 2422  $\text{km}^2$ ) [Rice et al., 2011], the Rio Grande headwaters, Colorado (3419  $\text{km}^2$ ) [Molotch, 2009], and the entire Sierra Nevada (60,000  $\text{km}^2$ ) [Rittger, 2012] found promising results. Also, the approach effectively explained the interannual variability of mean maximum SWE in the Tokopah Basin (19.1  $\text{km}^2$ ) in the southern Sierra Nevada, California, and the Green Lake 4 Valley (2.2  $\text{km}^2$ ) in the Front Range of Colorado over a 12 year period, with  $R^2$  values of 0.84 and 0.61, respectively [Jepsen et al., 2012].

[6] Application of the reconstruction approach to larger areas is limited by the difficulty of distributing model forcings over these scales and inaccuracies in larger scale snow-covered area (SCA) data products, but recent improvements in downscaling coarse spatial-resolution meteorological information (e.g., temperature, wind speed, relative humidity, and solar and thermal radiation) have enabled snowmelt simulations at regional scales [Andreadis and Lettenmaier, 2006; Durand et al., 2008; Molotch and Margulis, 2008]. Furthermore, improvements in detection of SCA from spaceborne platforms with daily temporal resolution [Painter et al., 2009; Rittger et al., 2013] afford

SWE reconstruction at larger scales, including the entire Sierra Nevada [Dozier, 2011]. While interpolation of sparsely distributed point SWE measurements over a large domain has limited utility for SWE estimation [Fassnacht et al., 2003], blending such measurements into the reconstruction may help constrain SWE estimates [Raleigh and Lundquist, 2012]. Such a blending approach may afford large-scale SWE estimation at previously unattained accuracy levels. Despite this potential, no study has blended surface observations of SWE with a SWE reconstruction model. Moreover, such a blending procedure may afford extension of the SWE reconstruction approach to larger spatial scales, e.g., mountain range scales ( $\sim 100,000 \text{ km}^2$ ). Accurately estimating SWE at these larger scales is critical for evaluating the hydrologic sensitivity to changes in climate [Christensen et al., 2004; Maurer, 2007], land cover change [VanShaar et al., 2002], and extreme weather events [Neiman et al., 2008]. Furthermore, such large-scale SWE estimates are critical for evaluating the terrestrial water balance via distributed models [Haddeland et al., 2011] and remotely sensed data [Niu et al., 2007; Syed et al., 2009].

[7] The objectives of the current study are (i) to evaluate the accuracy of the baseline reconstructed SWE estimates and the blended SWE estimates using  $\sim 3600$  in situ measurements, (ii) to illustrate the utility of the reconstructed and blended SWE estimation approaches by comparing with other SWE products in terms of accuracy and correlation with streamflow, and (iii) to characterize SWE distribution across the Sierra Nevada area at subwatershed resolution (15 arc second,  $\sim 500 \text{ m}$ ) using the reconstruction/blending approach described above. Data and methods are described in section 2. Results and validation are given in section 3. Section 4 addresses the sensitivity of the reconstruction and blending methods. Discussion of the results is given in section 5, followed by the conclusion in section 6.

## 2. Data and Methods

### 2.1. Study Area

[8] The 64,514  $\text{km}^2$  study area (Figure 1) covers 20 drainage basins that span the Sierra Nevada, 19 of which have full natural flow data (Table 1). Melt from the seasonal snowpack feeds rivers and recharges groundwater aquifers in the region. Most of the major rivers are located along the western slope of the mountain range, which flow westward to California's Central Valley. Mean elevation of the area is 1719 m, ranging from 30 to 4343 m. Mean forest density is 46% above 1500 m elevation (data described in section 2.2.2).

### 2.2. Data

#### 2.2.1. Snow Water Equivalent

[9] Ground truth SWE estimates were derived from carefully selected and timed snow surveys conducted at six sites (Figure 1, triangles) in the central and southern Sierra Nevada that represent areas of 16–20  $\text{km}^2$ . Surveys were conducted near the estimated date of maximum snow accumulation ( $\sim 1$  April of each year), and some surveys also took place in the middle of the melt season ( $\sim 15$  May of each year). About 3600 snow depth measurements were

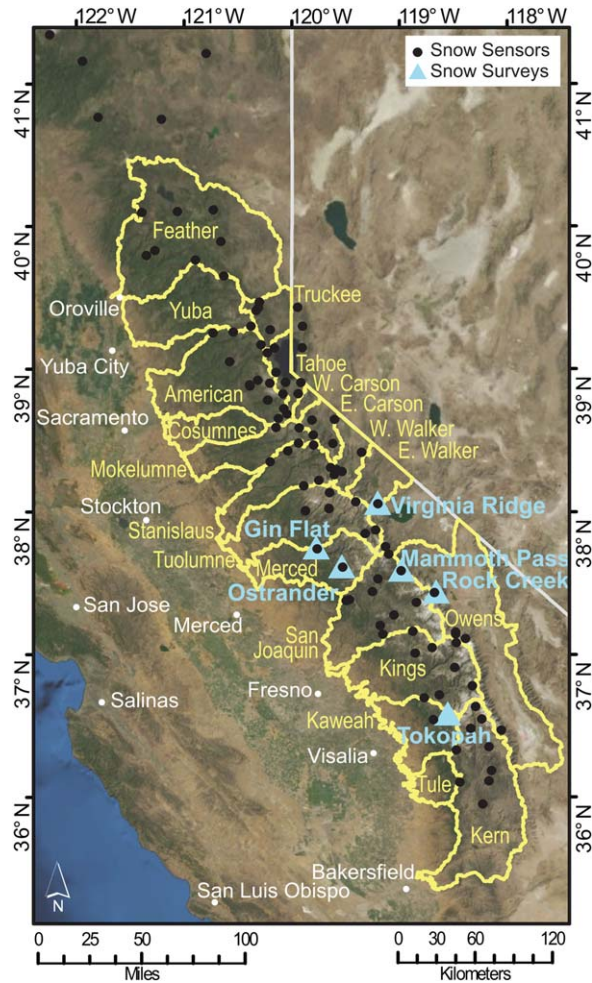


**Figure 1.** The study area consists of 20 watersheds (outlined by the yellow lines) in the Sierra Nevada, California. Snow survey (blue triangles) and snow sensor sites (black dots) are marked, as are major cities (white dots). Full natural flow data are available for 19 of the 20 watersheds (Table 1).

collected from 20 surveys during 2000–2009 and distributed to 30 m × 30 m pixels using two methods. A regression-tree model was used for sites other than the most southern site, Tokopah [Meromy *et al.*, 2012]. The regression tree model calculated gridded snow depths based on the snow survey observations and a variety of terrain-related independent variables derived from a digital elevation model (DEM) [Molotch and Bales, 2005; Molotch *et al.*, 2005a, 2005b]. The spatial density of the Tokopah surveys was not large enough to apply the regression-tree model, so gridded snow depths for this site were determined by linearly scaling the mean snow depths over 4 years (1996–1999) of intense surveys by the observed snow depths [Jepsen *et al.*, 2012, their Appendix B]. Gridded snow depths were multiplied by the mean observed snow density at each site to get gridded SWE, hereafter called the “snow survey SWE” that provides a best estimate of the spatial SWE variability over a heterogeneous terrain suitable for validating model performance.

[10] Operational SWE observations are provided by the California Department of Water Resources’ snow sensor

network (<http://cdec.water.ca.gov/>). Daily data from 104 snow sensor sites above 1500 m elevation (Figure 1, black dots) for the period of 2000–2012, hereafter called “snow sensor SWE,” are used both for the creation of blended SWE (described in section 2.4) and for model evaluation (as a secondary evaluation metric relative to snow surveys). Negative SWE values (which are physically unrealistic) are discarded. Note that validation and blending are performed independently via cross validation with these data.

[11] To compare reconstructed and blended SWE products to an existing SWE product, we use fine-resolution (1 km × 1 km) SWE over the contiguous US produced operationally by the Snow Data Assimilation System (SNODAS). SNODAS assimilates snow information from ground-based, airborne, and satellite platforms [Carroll *et al.*, 2001; Rutter *et al.*, 2008]. Its daily availability from 30 September 2003 provides a benchmark against which development of new SWE products should be compared [e.g., Rittger, 2012]. SNODAS ingests a variety of different sources of information, while information about snow extent is assimilated to mask daily estimates of SWE. Considerable underestimates in SWE may occur as satellite images assimilated into SNODAS do not account for snow beneath the forest canopy well [Barrett, 2003]. Also, SNODAS does not use information about snow cover depletion, and so comparisons with the reconstruction approach are needed.

**2.2.2. Snow-Covered Area**

[12] Images of fractional SCA ( $f_{SCA}$ ), the portion of each 500 m × 500 m grid cell covered with snow, are derived from spectral surface reflectance observations by the MODIS instrument [MODIS Snow-Covered Area and Grain size (MODSCAG): Painter *et al.*, 2009]. Multiple endmember spectral mixture analysis is used by MODSCAG to retrieve snow information over surfaces with complex structures. Daily images are masked by cloud cover information extracted from the standard MOD09

**Table 1.** Flow Gauges and Corresponding Watersheds in the Sierra Nevada

No.	Watershed	Flow Gauge	Drainage Area (km <sup>2</sup> )
1	Feather	Feather River at Oroville	9389.4
2	Yuba	Yuba River near Smartville	3871.3
3	American	American River below Folsom	5310.7
4	Cosumnes	Cosumnes at Michigan Bar	1680.0
5	Mokelumne	Mokelumne River at Pardee	2064.3
6	Stanislaus	Stanislaus River below Goodwin	2582.2
7	Tuolumne	Tuolumne River below La Grange	4184.3
8	Merced	Merced River below Merced Falls	2846.1
9	San Joaquin	San Joaquin River, Millerton	4418.7
10	Kings	Kings River below Pine Flat	4789.6
11	Kaweah	Kaweah River below Terminus	2428.5
12	Tule	Tule River below Success	1094.7
13	Kern	Kern River near Bakersfield	6141.6
14	Truckee	Truckee, Tahoe to Farad	1112.6
15	West Fork Carson	West Fork Carson at Woodfords	274.2
16	East Fork Carson	East Fork Carson near Gardnerville	900.1
17	West Walker	West Walker below Lake Walker	1054.3
18	East Walker	East Walker near Bridgeport	1303.5
19	Owens	Owens River below Long Valley	8107.6
20	Lake Tahoe	No full natural flow data	960.2

product based on Terra/MODIS and other sensors [Kotchenova *et al.*, 2006; Kotchenova and Vermote, 2007] and then manually screened for potentially nonretrieved cloud contaminations, with questionable images discarded. MODSCAG retrievals compare well with Landsat Thematic Mapper data in terms of accuracy [Rittger *et al.*, 2013], while their daily availability allows for more cloud-free images to be retained for each reconstruction. On average, 72 images are retained each year for the 6 month reconstruction period (March to August).  $f_{SCA}$  images are adjusted for canopy occlusion of snow cover, with corrected images given by

$$f_{SCA} = \frac{f_{SCA,MODSCAG}}{1 - f_{VEG}} \quad (1)$$

where  $f_{VEG}$  is percentage forest density [Molotch and Margulis, 2008]. It should be noted that the corrected images may still underestimate  $f_{SCA}$  depending on the forest density, with underestimates exceeding 40% at a heavily forested site (79% forest density) in the Sierra Nevada during the melt season [Raleigh *et al.*, 2013]. Forest density data are from the Global Forest Resources Assessment 2000 (FRA2000: <http://edc2.usgs.gov/glcc/fao/>). The 1 km  $\times$  1 km forest density data are interpolated to model resolution using cubic convolution. Cloud-contaminated  $f_{SCA}$  pixels and discarded  $f_{SCA}$  images are filled in by interpolating between the two nearest available images before and after the current time step, with cumulative potential snowmelt (see section 2.3) as the explanatory variable [Molotch, 2009].

### 2.2.3. Full Natural Flow

[13] Correlation with streamflow is used as an illustration of the potential utility of the SWE estimates to be produced. The magnitude of the streamflow is not an independent measurement of the total SWE volume, because of evaporation and transpiration of snowmelt and losses to groundwater before it reaches the stream gauges. Monthly full natural flow estimates for 19 rivers (Table 1) from the California Department of Water Resources (<http://cdec.water.ca.gov/snow/current/flow/fnfninfo.html>) account for upstream diversions, storage, and exchange of water with other watersheds.

### 2.2.4. Model Forcing

[14] Estimates of radiative (above-canopy insolation) and meteorological (precipitation, wind speed, air temperature, specific humidity, and surface air pressure) forcing for the SWE reconstruction model are provided by the North America Land Data Assimilation System Phase 2 (NLDAS: <http://ldas.gsfc.nasa.gov/nldas/>). The meteorological forcing is interpolated from NLDAS resolution (1/8 degree  $\times$  1/8 degree) to model resolution (15 arc second  $\times$  15 arc second) as follows: (1) the lapse rate (rate of change with height) of each forcing variable is calculated by regressing the variable (i.e., a spatial field) to topographic data from the Shuttle Radar Topography Mission [SRTM: Farr *et al.*, 2007] upscaled to NLDAS resolution, (2) the height-dependent part of each variable is linearly removed based on the lapse rate, (3) the residual part is bilinearly interpolated to model resolution, and (4) the height-dependent part is added back to the interpolated residuals to obtain the forcing variables at model resolution.

[15] NLDAS estimates of solar radiation over wavelength 0.2–3  $\mu\text{m}$  are downscaled using TOPORAD [Dozier, 1980; Dozier and Frew, 1990; Molotch and Margulis, 2008]:

$$S_{\text{downscaled},i} = \frac{S_{\text{TOPORAD},i}}{\frac{1}{K} \sum_{k=1}^K S_{\text{TOPORAD},k}} S_{\text{NLDAS}} \quad (2)$$

where  $S_{\text{NLDAS}}$  is the NLDAS estimate of solar radiation for a given NLDAS grid cell,  $S_{\text{TOPORAD},i}$  is the clear-sky solar radiation simulated by TOPORAD at pixel  $i$ ,  $K$  is the number of model pixels within the NLDAS grid cell, and  $S_{\text{downscaled},i}$  is the downscaled solar radiation. Mean root-mean-square (RMS) error in calculated downwelling shortwave radiation over the Tokopah Basin (located within our modeling domain) was 79  $\text{W m}^{-2}$  [Jepsen *et al.*, 2012]. The downscaled insolation is multiplied by a forest canopy solar transmission coefficient [Cline and Carroll, 1999] to get subcanopy insolation modulated by the FRA2000 forest densities. Snow albedo is calculated using the *US Army Corps of Engineers* [1956] (USACE) scheme.

[16] Upwelling longwave radiation is calculated using the Stefan-Boltzmann equation based on snow surface temperature, assumed to be the downscaled NLDAS 2 m air temperature one hour earlier or 0°C, whichever is colder [Cline and Carroll, 1999]. Snow emissivity is assumed to be 0.98 [Dozier and Painter, 2004]. Downwelling longwave radiation is from NLDAS, with corrections for forest canopy [Cline and Carroll, 1999].

## 2.3. Reconstruction Model

[17] For application to large domains, the SWE reconstruction model [Molotch, 2009] is modified to account for Earth curvature and varying solar geometry over the model domain. The model reconstructs peak SWE of each season by back-integrating snowmelt at each model step calculated from the energy balance at the snow surface and scaled by  $f_{SCA}$ . Snow depletion curves determined by cumulative potential snowmelt (i.e., assuming full snow coverage within a pixel) are used to interpolate  $f_{SCA}$  images over temporal gaps, and in turn convert potential snowmelt to actual snowmelt. Daily estimates of actual snowmelt are back-integrated from the period of satellite observed snow disappearance to the onset of snowmelt. The model domain covers Figure 1, with a zonal and meridional resolution of 15 arc second ( $\sim 500$  m), consistent with the resolution of MODIS snow cover observations. A total of 13 years (2000–2012) are reconstructed. For each year, the model covers the entire melt season at hourly time steps from 00:00 1 March to 23:00 31 August UTC.

[18] Potential snowmelt at each model pixel and each time step is calculated based on the following energy balance at the land surface:

$$M_p \rho L = S \downarrow (1 - \alpha) + LW \downarrow + LW \uparrow + SH + LH \quad (3)$$

where  $S \downarrow$  is the subcanopy insolation,  $\alpha$  is snow albedo,  $LW \downarrow$  is the downwelling longwave radiation,  $LW \uparrow$  is the longwave radiation emitted from the snowpack,  $SH$  is the sensible heat exchange,  $LH$  is the latent heat exchange,  $\rho$  is the density of liquid water,  $L$  is the latent heat of fusion, and  $M_p$  is the potential melt; fluxes toward (away from) the

snow surface are considered positive (negative). Sensible and latent heat fluxes are calculated from wind speed, temperature, and relative humidity [Jordan, 1991], with stability adjustment based on the sign of the bulk Richardson number [Liston et al., 1999]. Turbulent fluxes are not corrected for canopy, the effect of which is expected to be insignificant in this application given that turbulent fluxes account for a relatively small fraction of the snowmelt energy (10% on average in the Tokopah Basin) [Jepsen et al., 2012]. The right side of the equation gives the maximum possible energy available for melting snow. Potential melt is scaled by  $f_{SCA}$  of the pixel to obtain actual melt during a time step:

$$M = M_p \times f_{SCA} \quad (4)$$

[19] The ablation season mass balance of the snowpack can be approximated by

$$SWE_n = SWE_0 - \sum_{j=1}^n M_j \quad (5)$$

where  $SWE_n$  is SWE at time step  $n$ ,  $SWE_0$  is the initial SWE, and  $M_j$  is the actual melt during time step  $j$ . The initial SWE at each model pixel can be reconstructed at the time when  $f_{SCA}$  indicates snow disappearance:

$$SWE_0 = \sum_{j=1}^n M_j, \text{ when } SWE_n = 0 \quad (6)$$

[20] SWE at each model time step can be obtained henceforth by using equation (5). SWE values at 06:00 UTC daily (following SNODAS) are extracted. This daily SWE product is the subject of subsequent validation analysis and is hereafter called the “reconstructed SWE.”

[21] With no systematic biases in equation (5), overestimates of reconstructed peak SWE will be determined by the amount of snow accumulation during the melt season. For each year of 2004–2012, snowfall after peak SWE accounts for 4%, 8%, 2%, 25%, 5%, 17%, 10%, 10%, and 3% of the total seasonal snowfall in the Sierra Nevada above 1500 m elevation based on the SNODAS input snowfall data. In some years, especially 2007 and 2009, it is one of the main error sources.

#### 2.4. Blending of Reconstructed and Observed SWE

[22] Snow sensor SWE is blended with reconstructed SWE for each day to constrain the retrieval. The difference between reconstructed and observed SWE at each snow sensor site is distributed to all model pixels using the inverse of the squared distance as distribution weights [Molotch et al., 2005a, 2005b]. Blended SWE is produced by subtracting the distributed residuals from reconstructed SWE:

$$SWE_{blended,l} = SWE_{reconstructed,l} - \frac{\sum_{k=1}^N SWE_{residual,k} \frac{1}{D_{l,k}^2}}{\sum_{k=1}^N \frac{1}{D_{l,k}^2}} \quad (7)$$

where  $SWE_{blended,l}$  is blended SWE at pixel  $l$ ,  $SWE_{reconstructed,l}$  is reconstructed SWE at pixel  $l$ ,  $SWE_{residual,k}$  is the difference

between reconstructed and observed SWE at snow sensor site  $k$ ,  $D_{l,k}$  is the distance between pixel  $l$  and snow sensor site  $k$ , and  $N$  is the number of available snow sensor sites. The blended SWE is set to zero where the MODIS-based  $f_{SCA}$  is zero, keeping the final estimate consistent with the satellite-observed snow extent. When all sensors report zero SWE, the blended product becomes a smoothed version of reconstructed SWE.

#### 2.5. Evaluation Method

[23] In situ observations of two types are used to evaluate reconstructed and blended SWE. (i) Snow survey SWE, with high-resolution spatial sampling, is best suited for validating the model results. However, these manually intensive snow surveys are limited in number and location. (ii) Snow sensor SWE values are from spatially sparse “point” observations, and hence represent “truth” less well at model resolution; but they are distributed across the model domain. Moreover, their daily availability enables assessment of the temporal evolution of model errors. Because of the discrepancy in their representative spatial scales, model evaluation with these snow sensor data is expected to be less robust than evaluation with the snow survey data.

[24] To facilitate comparison, snow survey SWE (30 m × 30 m) and reconstructed/blended SWE (about 500 m × 500 m) are upscaled to SNODAS resolution (about 1 km × 1 km) by averaging within each SNODAS pixel. Statistics are calculated and compared between different SWE products over the common grid.

[25] Cross validation [Carroll and Cressie, 1996; Erxleben et al., 2002; Fassnacht et al., 2003; Luzio et al., 2008] is used to evaluate blended SWE over snow sensor sites; blended SWE equals snow sensor SWE at each snow sensor site, by definition. To evaluate the accuracy at these sites, the blending procedure is repeated many times by leaving out each snow sensor site iteratively. For the omitted site, blended SWE is obtained from residual SWE calculated from the remaining snow sensor sites. The procedure is repeated until blended SWE values are obtained for all snow sensor sites independent of the observed SWE at the individual site. This ancillary data set is called the “cross-validated blended SWE.”

### 3. Results

#### 3.1. Evaluation With Snow Survey Data

[26] Relative to snow survey SWE, reconstruction underestimates mean SWE in all but one of the cases (Figure 2, red dots). For blended SWE, underestimates and overestimates occur in 8 and 12 cases, respectively. Underestimates occur in SNODAS SWE in all but one of the cases. Blended SWE has smaller RMS errors than does reconstructed SWE in 15 out of the 20 cases. Among the 17 cases when SNODAS data are available, RMS errors are smaller in reconstructed SWE than in SNODAS SWE in six cases and are larger in the other 11 cases. In comparison, RMS errors are smaller in blended SWE than in SNODAS SWE in nine out of the 17 cases. Error statistics averaged over the 17 cases are given in Table 2. It should be noted that most snow surveys are near a snow sensor site (see Figure 1) that was ingested into SNODAS but not into reconstructed SWE. Noteworthy are the Tokopah

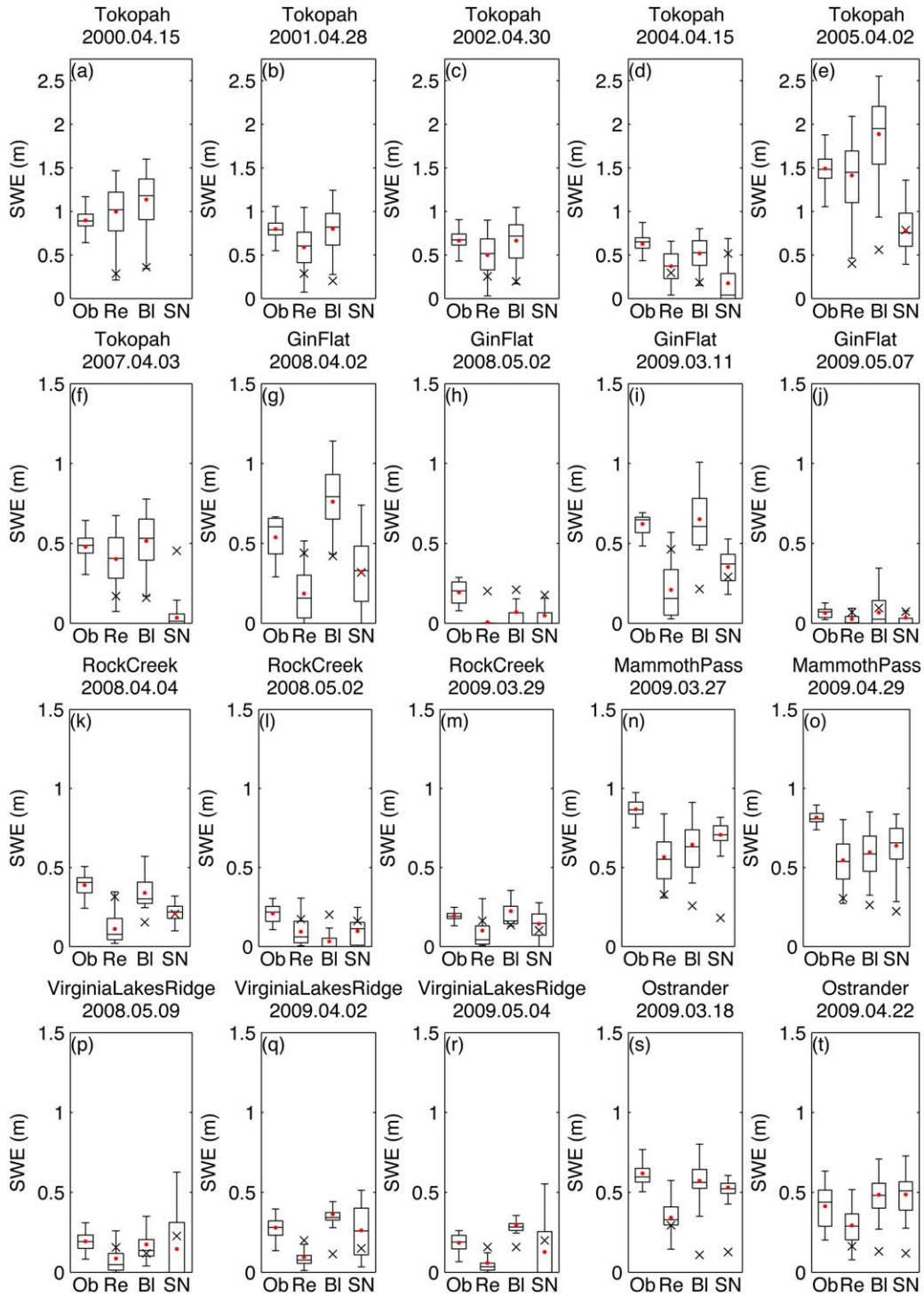


**Figure 2.** Box-and-whisker plots of snow survey (Ob), reconstructed (Re), blended (BI), and SNODAS (SN) SWE (m). Whiskers are drawn one interquartile range (IQR) below the first quartile and one IQR above the third quartile. Outliers, if any, are not shown. Red dots indicate the means. X-marks show the RMS error of reconstructed, blended, and SNODAS SWE compared to snow survey SWE. Snow survey sites (see Figure 1, blue triangles) and dates are indicated in the plot titles. SNODAS data are not available until 2003, and so are missing in Figures 2a–2c.

surveys, which are not near a snow sensor site. Validation with the Tokopah surveys shows that both reconstructed and blended SWE are consistently more accurate than SNODAS SWE (Figures 2d–2f).

**3.2. Evaluation With Snow Sensor Data**

[27] Figure 3 compares April 1 SWE with snow sensor SWE, reconstructed SWE, *cross-validated* blended SWE (section 2.5), and SNODAS SWE for 13 years. For snow

**Table 2.** Mean Bias, Mean Absolute Error, and RMS Error (m) of Reconstructed, Blended, and SNODAS SWE Averaged Over 17 Snow Surveys<sup>a</sup>

	Reconstructed	Blended	SNODAS
Mean bias	-0.193 (-40.0%)	0.001 (0.2%)	-0.181 (-37.7%)
Mean absolute error	0.226 (47.0%)	0.170 (35.4%)	0.223 (46.4%)
RMS error	0.252 (3.3 $\sigma$ )	0.205 (2.7 $\sigma$ )	0.254 (3.3 $\sigma$ )

<sup>a</sup>Normalized mean bias and mean absolute error (in percentage of mean snow survey SWE), and normalized RMS error (in units of the standard deviation of the snow survey SWE,  $\sigma$ ) are given in the brackets.

sensors, the values are averages over all sites. For others, the values are averages over those pixels with a snow sensor site inside. Reconstructed April 1 SWE is smaller than the snow sensor observation in 11 out of the 13 years. The two are closer in 2000, 2003, 2006, and 2010 when their difference is within 9% of snow sensor SWE. Blended April 1 SWE is almost identical to snow sensor observations (within 4%) in all 13 years. SNODAS compares well with snow sensor observations in most years, the exception being 2007 when SNODAS SWE is smaller than snow sensor SWE by about 30%.

[28] Figure 4 compares daily time series of mean reconstructed and snow sensor SWE, averaged over all snow sensors. RMS errors and spatial correlations are calculated between snow sensor sites and model pixels with a snow sensor site inside. Mean SWE is underestimated in most reconstructions, the main exception being the 2006 reconstruction, when heavy snowfall occurred in March and early April. Mean SWE bias is smallest during 2000, when reconstructed SWE closely matches observed SWE throughout the reconstruction period. For other years, seasonal maximum bias in mean SWE is between 30% and 61% of April 1 snow sensor SWE. RMS errors and correlations between reconstructed and snow sensor SWE are stable over the beginning few months of the melt season. RMS errors gradually decrease to zero as snow disappears, which is not unexpected as both reconstructed and observed SWE approach zero. Reconstructed and observed SWE become uncorrelated near the end

of the melt season, when there is little snow on the ground. Earlier, the correlation is reasonably high, ranging  $\sim 0.4$ – $0.8$ . The maximum RMS error each year ranges from 1.2 to 1.7 standard deviations of the April 1 snow sensor SWE.

[29] Figure 5 shows error statistics for the cross-validated blended SWE (section 2.5). The mean value of blended SWE is almost identical to snow sensor observations throughout the melt season, which is desired but not trivial given that at each snow sensor the blended SWE value is obtained independently of the observed SWE at that sensor. RMS errors are reduced considerably in all years relative to reconstructed SWE. Correlations are also larger, in general, although the improvements are not as prominent as in RMS errors. The maximum RMS error each year is reduced to 0.8–1.2 standard deviations of the April 1 snow sensor SWE.

[30] Similar error statistics are calculated for SNODAS SWE for the 9 years when SNODAS data are available, shown in Figure 6. Mean SNODAS SWE follows snow sensor observations in most years, with seasonal maximum bias ranging between 10% and 20% of April 1 SWE; the exception being year 2007 when maximum bias reaches 46% of April 1 SWE. These biases are considerably higher than in the case of blended SWE (Figure 5), where maximum bias is within 6% of April 1 SWE during all years. Correlations are larger than in the case of blended SWE. The maximum RMS error each year is 0.6–0.9 standard deviation of the April 1 snow sensor SWE. The blended SWE value at each snow sensor site is obtained without observed SWE information from that site, while snow sensor SWE is assimilated in SNODAS. A truly equal comparison would involve omitting each snow sensor from the SNODAS SWE estimation procedure and then comparing the SNODAS SWE estimate with the observed SWE. Doing so is not possible because we do not have the SNODAS code, but we presume the errors would be greater. Hence, the quality of the blended SWE product relative to SNODAS is probably greater than reported in this subsection, as already suggested by the snow survey based evaluation in section 3.1 where the comparisons are more representative of SNODAS errors relative to blended SWE.

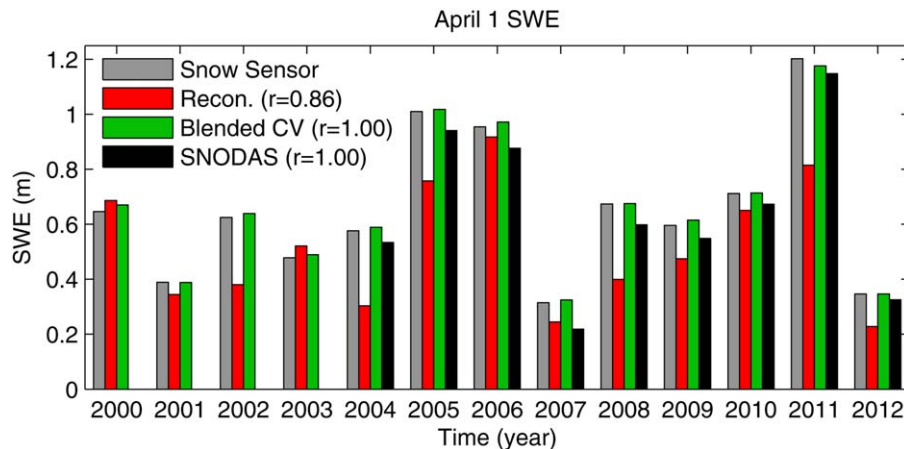


**Figure 3.** Snow sensor, reconstructed, blended (cross validated), and SNODAS SWE (m) on April 1 every year during 2000–2012, averaged over all snow sensor sites (see Figure 1, black dots). Correlations between snow sensor SWE and the latter three are shown in the legend.

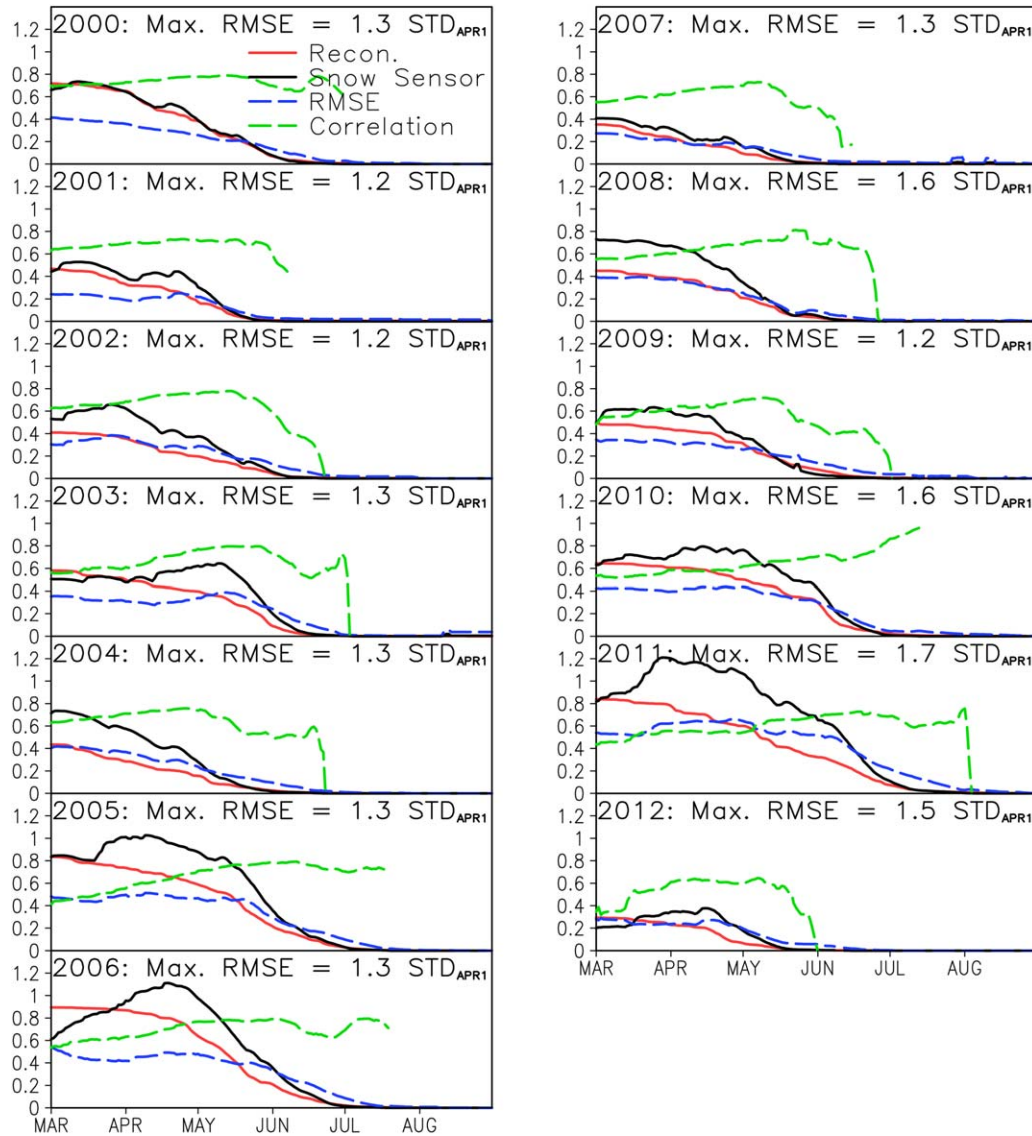


**Figure 4.** Mean SWE (m), averaged over all snow sensor sites (see Figure 1, black dots), is shown for the reconstruction (red) and for the snow sensor observation (black). Also shown are the RMS errors of the reconstruction relative to the observation (blue), and the correlation between the reconstruction and the observation (green). The maximum RMS errors each year, shown in units of the standard deviation of the observed April 1 SWE, vary from 1.2 to 1.7.

### 3.3. Spatial SWE Differences

[31] Spatial April 1 SWE is compared between reconstructed, blended, and SNODAS SWE (Figure 7). The overall pattern of the SWE differences is similar from year to year. Therefore, only 2 representative years, one relatively wet and one relatively dry, are shown along with the mean difference over the comparison period (2004–2012).

[32] Reconstructed SWE is less than SNODAS by up to 2.00 m and greater than SNODAS by up to 2.81 m during the wet year of 2005. SWE differences are  $\sim 1/3$ – $1/2$  as large during the dry year of 2007. The mean difference over 2004–2012 lies between the 2 extreme years, ranging from  $-1.03$  to  $2.04$  m (Figure 7, top row). Spatially, reconstructed SWE is predominantly less than SNODAS over the southern two thirds of the Sierra Nevada along the western slope and greater than SNODAS in the northern-

most watersheds. High reconstructed SWE in the heavily forested northern watersheds may be related to the correction for viewable gap fractions applied to  $f_{SCA}$  maps. In that regard, reconstructed SWE can be significantly larger than SNODAS because the approach estimates subcanopy  $f_{SCA}$  based on observed  $f_{SCA}$  within viewable gaps (i.e., open areas).

[33] Blended SWE is greater than SNODAS SWE over the majority of the domain (Figure 7, middle row). SWE differences range from  $-1.64$  to  $2.86$  m during 2005, from  $-0.64$  to  $2.08$  m during 2007, with the 2004–2012 mean differences in between. Blending with snow sensors considerably reduces the negative difference between reconstructed and SNODAS SWE over the southern two thirds of the Sierra Nevada. In this regard, blending the reconstructed SWE with snow sensors affects the southern part

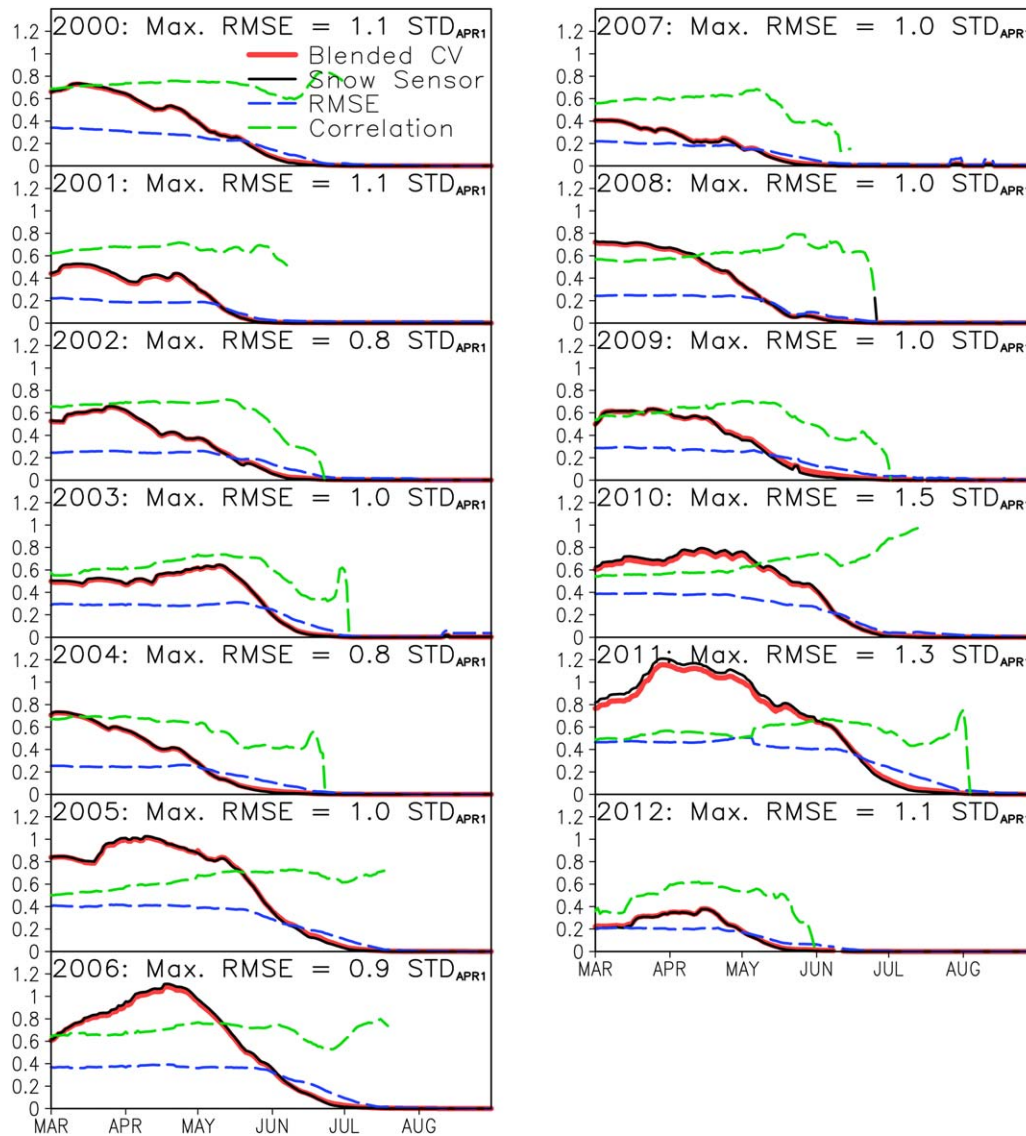


**Figure 5.** As Figure 4 except for the cross-validated blended SWE (m).

more than the northern part of the Sierra Nevada (Figure 7, bottom row, which effectively shows the distributed residuals of the reconstructed SWE). It remains to be understood what factors (e.g., elevation, forest density, and distribution of snow sensors) determine the spatial pattern of the residuals of the reconstructed SWE.

**3.4. Streamflow Correlations**

[34] Shown in Figure 8 are interannual correlations between full natural flow and the four SWE data sets over 19 watersheds. Correlation is calculated between April to July total flow and annual peak SWE, as well as between monthly flow and SWE changes ( $\Delta$ SWE), for each watershed. For monthly flow,  $\Delta$ SWE over the current and the preceding month is used in the calculation to accommodate some delayed response in streamflow to snowmelt.

[35] Statistical correlations between peak SWE and April to July full natural flow are consistently greater for reconstructed SWE versus other SWE data sets; significant at

the 95% level among 15, 18, 16, and 17 out of the 19 watersheds for observed, reconstructed, blended, and SNODAS SWE. Correlation ( $r$ ) values average to 0.85, 0.91, 0.81, and 0.86 for the four data sets, respectively (Figure 8a). Reconstructed SWE better correlates with seasonal streamflow than does snow sensor SWE over 14 out of the 19 watersheds, and better than does SNODAS SWE over 17 out of the 19 watersheds. Relatively low correlations with blended SWE tend to occur where correlations with snow sensors are low (Feather, Tule) or where no snow sensors are present (Cosumnes). On the other hand, missing or low correlations of streamflow with snow sensors do not necessarily relate to low correlations of streamflow with blended SWE (Kaweah, West Fork Carson). Correlation with blended SWE over the Cosumnes and West Fork Carson watersheds, with no snow sensors, is similar to the correlation with SNODAS SWE. Correlations with reconstructed and blended SWE are greater than with SNODAS in the northern portions of the Sierra Nevada (i.e., Feather, Yuba,

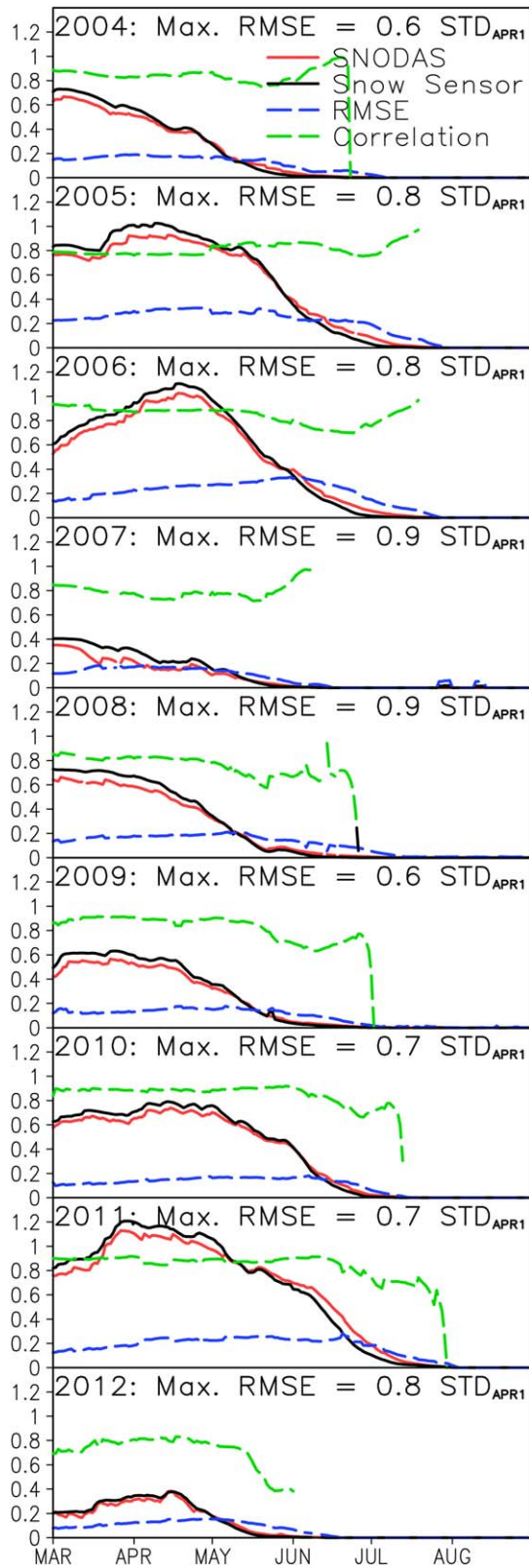


**Figure 6.** As Figure 4 except for SNODAS SWE (m). Comparisons are not made before year 2004 because data were unavailable.

American). These basins are particularly important for the California State Water Project, and thus these snow products may be particularly relevant for water resource studies in these basins.

[36] Of particular interest are the later months of the melt season (June and July) when snow has melted in the lower elevations. Many snow sensors show zero SWE during these months, while in fact there is still snow in the higher elevation not covered by the current snow sensor network, as *Rice et al.* [2011] also show. Figure 9 illustrates the unrepresentative sampling of the snow sensor network, showing the elevation histogram of all model pixels versus those pixels with collocated snow sensors. As seen, the

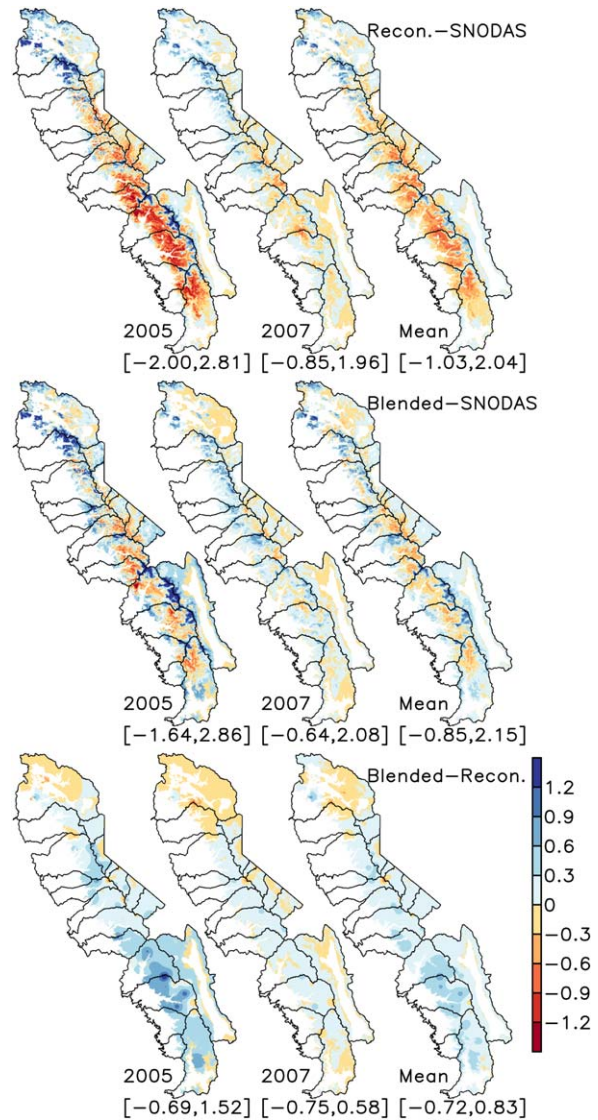


**Figure 7.** Difference in April 1 SWE (m) between (top) reconstructed SWE and SNODAS SWE, (middle) blended and SNODAS SWE, and (bottom) blended and reconstructed SWE. (left) 2005, (center) 2007, and (right) the mean over 2004–2012. In each plot, the range of the SWE difference (which is larger than the color bar limit) is indicated in the square brackets under the year label. Watershed boundaries are shown by the black lines.

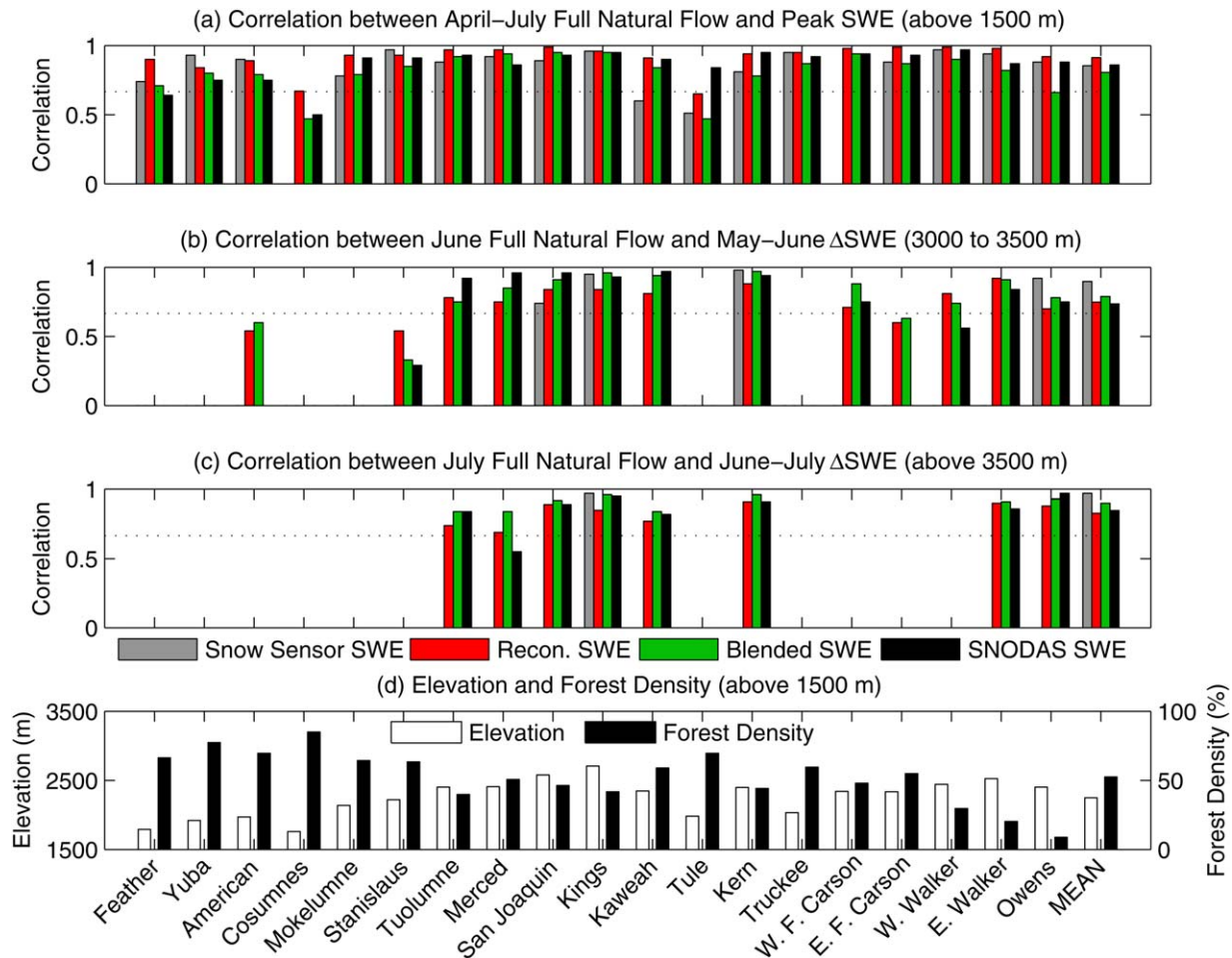


**Figure 8.** (a) Correlation between April to July total full natural flow and annual peak SWE above 1500 m elevation over 19 watersheds. (b) Correlation between June flow and May to June  $\Delta$ SWE for the 3000–3500 m elevation band. (c) Correlation between June flow and May to June  $\Delta$ SWE above 3500 m elevation. (d) Mean elevation (m) and forest density (%) above 1500 m elevation. In each plot, the mean over the 19 watersheds is shown by the rightmost group of bars. Correlations are for year 2004–2012, with the dotted lines showing the 5% significance level based on a two-tailed test.

snow sensor network has a better coverage over the middle elevations, whereas limited representation of the lower and higher elevations exists. Thus, during later months, the number of snow sensors available to distribute SWE residuals as part of the SWE blending procedure is much reduced. The method nonetheless appears to remain effective during later months as natural streamflow correlations are higher with blended SWE than with snow sensor, reconstructed, and SNODAS SWE in the majority of the cases (Figures 8b and 8c). Reconstructed SWE, which has no reliance on in situ measurements, also shows high correlations in most cases during these months, although in general lower than blended SWE. On the other hand, correlations cannot be obtained between snow sensor SWE and streamflows over the majority of the watersheds since few snow sensors are present over the higher elevations. It is important to note that basins showing high correlations between streamflow and reconstructed/blended SWE in July (Figure 8c) correspond with higher elevations (Figure 8d).

[37] Similar correlation values to those in Figure 8 can be obtained when SWE outside the snow sensor elevation range is not counted, suggesting that the contrasts in streamflow correlations for snow sensor SWE versus other SWE products are not merely a result of the inclusion of SWE at higher and lower elevations in the other products but reflect the differences between these SWE products.

### 3.5. Spatial and Interannual Variability of SWE

[38] Figure 10 (all except the lower right plot) shows the spatial distribution of April 1 SWE percent anomalies for Sierra Nevada elevations greater than 1500 m based on blended SWE. The 13 year mean (Figure 10, lower right plot) is removed from each model pixel to form SWE anomalies. The 13 year mean SWE is characterized by maximum values on the west side of the Sierra crest. Above-average SWE is most prominent during 2005, 2006, and 2011. Below-average SWE is seen throughout the Sierra Nevada during 2001, 2007, and 2012. The spatial pattern of SWE anomalies varies from year to year. For

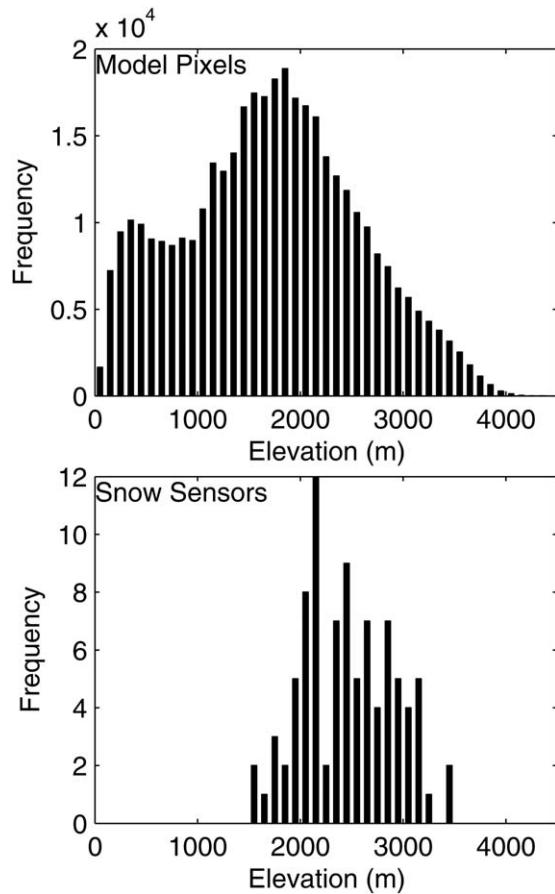


**Figure 9.** Elevation histogram for (top) all model pixels and (bottom) snow sensor sites (Figure 1, black dots).

example, SWE anomalies are larger in the southern portion than in the northern portion of the Sierra Nevada during 2005, whereas larger SWE anomalies are seen in the north than in the south during 2001, which could be related to the position and strength of the storm track. Variability on watershed and subwatershed scales is also evident. Domain SWE is above the 13 year mean in 2005, 2006, and 2011, below the 13 year mean in 2001, 2003, 2007, and 2012, and close to the 13 year mean in other years (Figure 11). Spatial SWE variability is larger in the drier years than in the wetter years, according to the coefficient of variation (not shown). The interannual spatial patterns in SWE anomalies have implication for identifying the source of water supply forecast errors associated with point-based unrepresentative sampling and for identifying locations for future snow sensor network expansion [e.g., Welch et al., 2013].

### 3.6. Domain-Averaged SWE

[39] Figure 12 shows domain-averaged SWE within the entire Sierra Nevada where elevation is greater than 1500 m, based on the four data sets: snow sensor, reconstructed, blended, and SNODAS SWE. Model-interpolated  $f_{SCA}$  is also shown at 7 day intervals. Note that the snow sensor average does not attempt to characterize the magnitude of basin SWE, which will require careful interpolation of the observed SWE values across the domain. Notable differ-

ences can be seen between the four domain-averaged SWE estimates (SNODAS is not available during the first 4 years compared), especially near peak accumulation. The snow sensor estimate is expectedly higher given the inadequate spatial sampling, unrealistic representation of the elevation distribution (Figure 9), and the tendency of the snow sensors being placed in locations with higher SWE [Molotch and Bales, 2005; Newald and Lehning, 2011]. It is the highest among the four estimates, except near the end of the melt season when many snow sensors show zero SWE while there is still snow in the higher elevations, as discussed in section 3.4. It is larger than the reconstruction-based estimate by roughly a factor of two around the time of peak accumulation during most years. The estimate based on blended SWE falls between the snow sensor observation and reconstruction, because the residuals between snow sensor and reconstructed SWE tend to be positive (i.e., the model underestimates SWE), and therefore blended SWE (which is based on these residuals and their interpolation) is larger than reconstructed SWE. Peak SWE in SNODAS is considerably smaller than in blended SWE in most years. The different data sets show interesting temporal characteristics. For example, reduction of snow cover and SWE is rapid in 2001 and 2003 about 1 month before snow disappears. While SWE reduction is also quick in 2005 and 2006, the snow cover follows a more gradual depletion curve. Year 2006 stands out because of that year's large snowfall in March and early April. SWE steadily increases from the beginning of March that year to about double its initial amount in  $\sim 1.5$  months, as seen in snow sensor, blended, and SNODAS SWE, while snow covered area is relatively stable during this period.

## 4. Sensitivity Tests

[40] The sensitivity of reconstructed SWE is tested for the following four aspects of the reconstruction model that have the largest uncertainties: downwelling longwave radiation, snow albedo, forest density, and turbulent fluxes. In the control runs, NLDAS downwelling longwave radiation, the USACE albedo algorithm, and FRA2000 forest density data were used, and turbulent fluxes (i.e., sensible plus latent) were explicitly calculated (section 2.3). For the sensitivity test, downwelling longwave radiation is calculated from downscaled NLDAS 2 m air temperature, where clear-sky atmospheric emissivity is derived from 2 m air temperature and water vapor pressure [Idso, 1981; Hodges et al., 1983; Jordan, 1991] with corrections for forest canopy [Cline and Carroll, 1999]. This longwave scheme performed reasonably well in the Tokopah Basin (located within our modeling domain) with mean RMS error of  $28 \text{ W m}^{-2}$  [Jepsen et al., 2012]. For albedo, the Biosphere Atmosphere Transfer Scheme (BATS) [Dickinson et al., 1993] is used in the sensitivity test. Molotch and Bales [2006] showed that this albedo scheme performed better than the USACE scheme in the Tokopah Basin, but neither scheme accounts for spatial variability of albedo decay. Forest density from the National Land Cover Dataset (NLCD) 2001 is tested, which has a 30 m spatial resolution. For turbulent fluxes, the restricted degree-day method [Brubaker et al., 1996; Molotch and Margulis, 2008] is tested. Unlike in the control run where sensible and latent heat

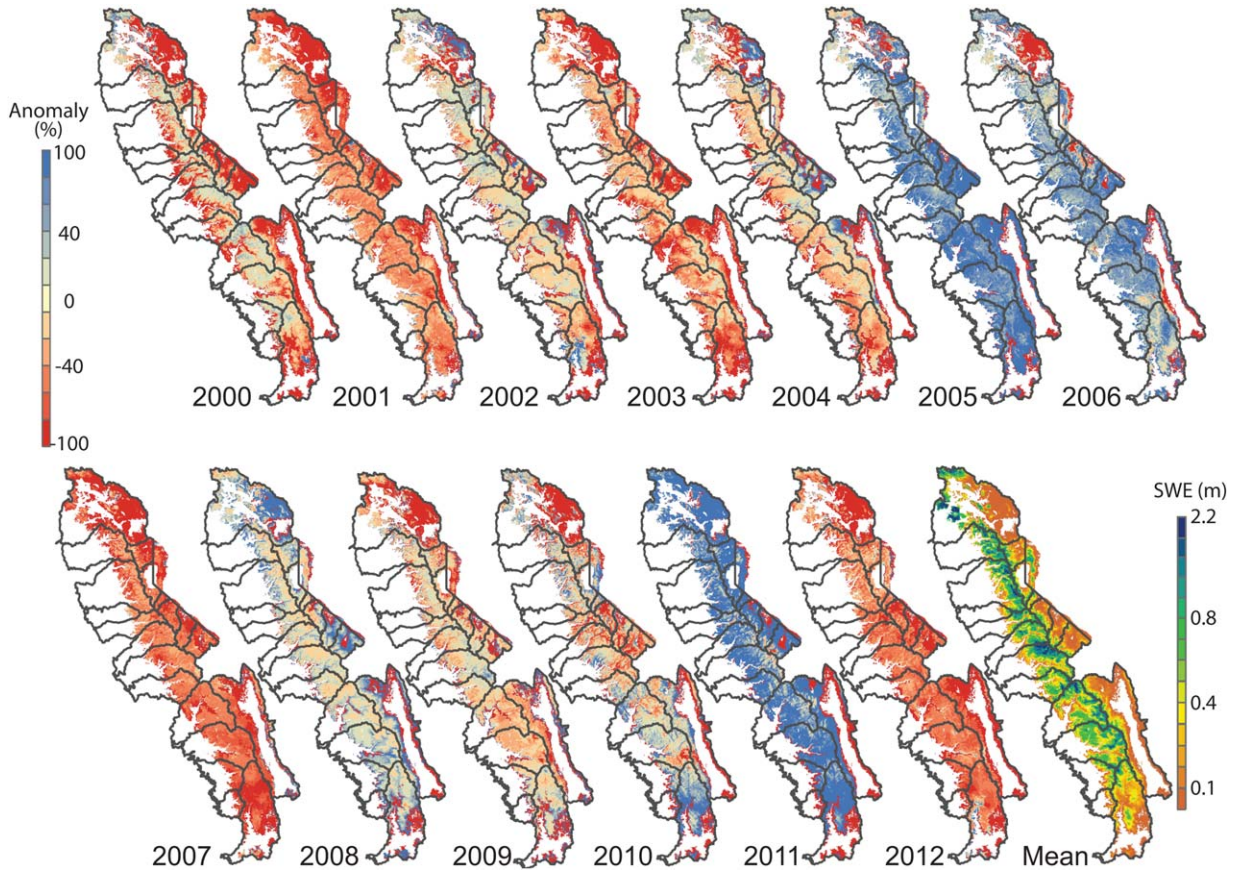


**Figure 10.** April 1 SWE percent anomalies, as computed by the blended SWE, each year during 2000–2012 (first 13 plots) relative to the 13 year mean April 1 SWE (lower right plot). Data for the 20 watersheds cover only pixels above 1500 m elevation.

fluxes are explicitly calculated, this method parameterizes the bulk turbulent fluxes based on temperature and a degree-day coefficient. Three different values of the degree-day coefficient [Molotch *et al.*, 2010] are tested, representing their potential range. The tests are performed for the year 2009, for which in situ SWE from nine snow surveys in the Sierra Nevada are available.

[41] Error statistics of reconstructed SWE from these test runs relative to snow survey SWE are given in Table 3. Error statistics are similar to the control run when *Idso* [1981] longwave or the degree-day method with a coefficient value of  $0.15 \text{ cm } ^\circ\text{C}^{-1} \text{ day}^{-1}$  is used. Errors are slightly larger than the control run when BATS albedo is used, somewhat expected because the BATS algorithm may overestimate albedo [Warren and Wiscombe, 1980; Jin *et al.*, 1999]. Errors are largest in the case of NLCD forest density and smallest in the case of a degree-day coefficient of 0.30. Larger errors based on NLCD forest density compared to the control suggests that either FRA2000 used in the control is more accurate despite the coarser spatial resolution (1 km versus 30 m), or FRA2000 is less accurate than NLCD but there are compensating errors from the model. Considering mean reconstructed SWE over the nine snow surveys, the difference based on the two forest density products is 0.06 m, and the difference based on a reasonable perturbation to the degree-day coefficient (i.e., from 0.15 to 0.20) is 0.05 m (Table 3, the row for mean

bias). The above sensitivity in reconstructed SWE is equivalent to about  $10 \text{ W m}^{-2}$  mean bias in net radiation above

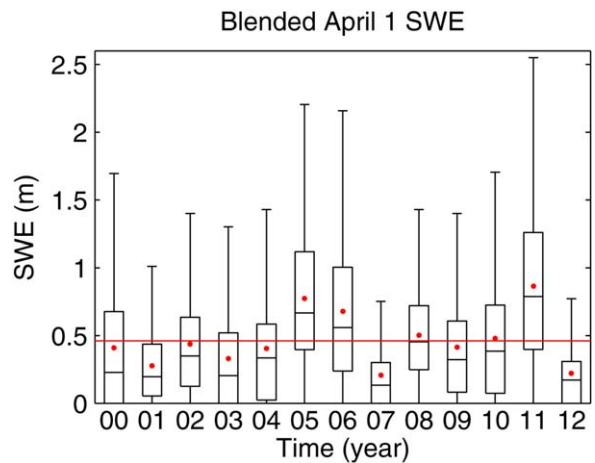


**Figure 11.** Box-and-whisker plot of blended April 1 SWE. Statistics are based on all available pixels in the Sierra Nevada above 1500 m elevation. Whiskers are drawn one interquartile range (IQR) below the first quartile and one IQR above the third quartile. Outliers, if any, are not shown. Red dots indicate the means, and the red line indicates the 13 year mean.

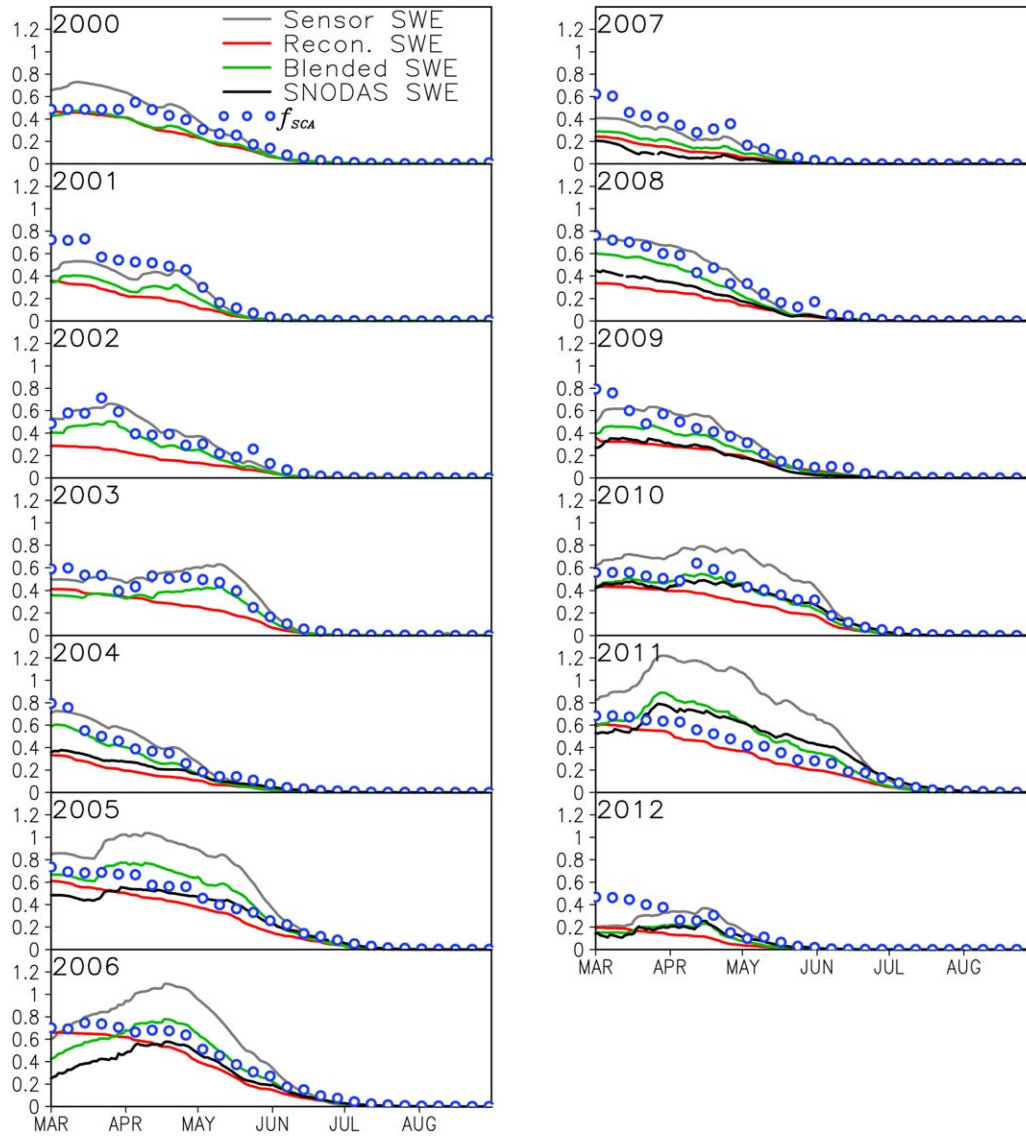


**Figure 12.** Domain-averaged SWE (m) based on snow sensor, reconstructed, blended, and SNODAS SWE. Model-interpolated  $f_{sca}$  is also shown at 7 day intervals, for reference. For snow sensor SWE, averaging is done over all available sensor sites in the Sierra Nevada (Figure 1, black dots). For others, averaging is over all available model pixels in the Sierra Nevada with elevation greater than 1500 m.

the snow surface. For reference, input downwelling solar radiation to the reconstruction model (i.e., downscaled NLDAS) has a mean bias of about  $-10 \text{ W m}^{-2}$  evaluated over 11 sites in the Sierra Nevada during 5 years (not shown). Using a temperature index model, Slater *et al.* [2012] estimated a 5 day error in the date of snow disappearance or one degree error in air temperature is compara-

ble to  $13 \text{ W m}^{-2}$  error in net radiation in terms of the bias produced in reconstructed SWE. The test here suggests the sensitivity of reconstructed SWE to errors in forest density products and degree-day coefficient values is comparable to the sensitivity of reconstructed SWE to typical magnitude of errors in the time of snow disappearance and air temperature in such applications. We do not account for the

**Table 3.** Mean Bias (m), Mean Absolute Error (m), and RMS Error (m) of SWE From the Sensitivity Tests, Averaged Over Nine Snow Surveys in Year 2009

	Control	Idso Downward Longwave	BATS Albedo	NLCD Forest Density	Degree Day (0.15 <sup>a</sup> )	Degree Day (0.20 <sup>a</sup> )	Degree Day (0.30 <sup>a</sup> )
Mean bias	-0.20	-0.18	-0.22	-0.26	-0.20	-0.15	-0.05
Mean absolute error	0.22	0.21	0.24	0.28	0.23	0.20	0.18
RMS error	0.25	0.24	0.26	0.31	0.26	0.23	0.22

<sup>a</sup>Unit:  $\text{cm } ^\circ\text{C}^{-1} \text{ day}^{-1}$ .

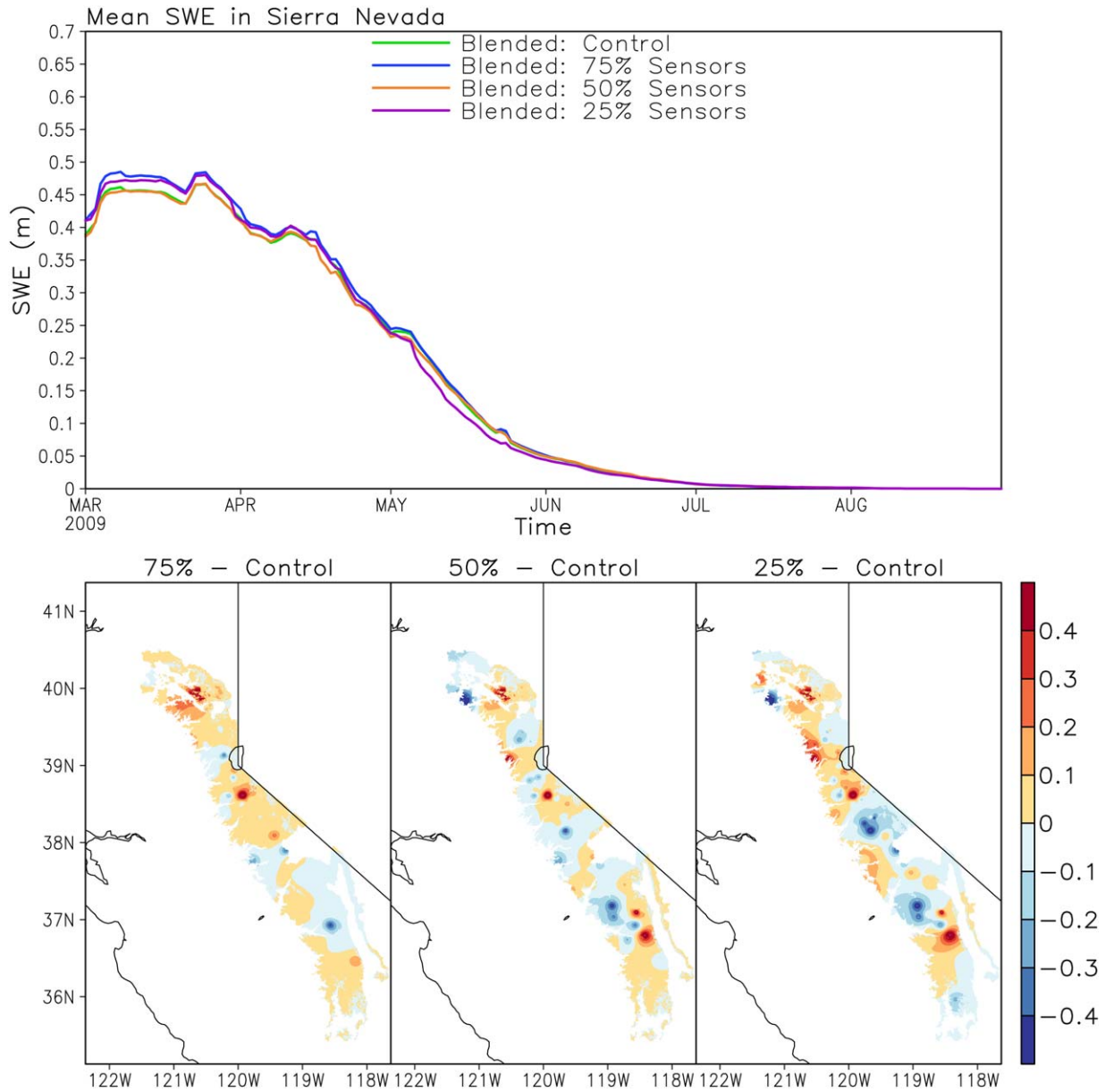


**Figure 13.** Sensitivity of blended SWE to the number of snow sensors used. (top) Mean SWE (m) in the Sierra Nevada based on four blended SWE products where all (control), 75%, 50%, and 25% of the snow sensors are used for blending with the reconstructed SWE. (bottom) April 1 SWE (m) differences between the latter three products and the control.

likely spatial variability of the degree-day coefficient [Kumar *et al.*, 2013]. The relative magnitudes of the error statistics in Table 3 suggest the four aspects tested (i.e., downwelling longwave radiation, snow albedo, forest density, and turbulent fluxes) are all potentially important sources of errors and uncertainties in reconstructed SWE.

[42] To assess the applicability of the blended method for other applications where snow sensor observations are less available, sensitivity tests are done where 75%, 50%, and 25% of the available sensors are randomly selected for blending. Mean SWE from these tests closely follow the control throughout the melt season (Figure 13, upper plot). The sensitivity in mean SWE is relatively small compared to the magnitude of mean SWE. Spatially, blended SWE from the sensitivity tests are within 0.1 m of the control

over the majority of the domain. As the number of sensors retained is reduced, local differences in blended SWE become greater. SWE differences rarely exceed 0.1 m when 50–75% of the sensors are retained but become considerably larger when only 25% of the sensors are retained.

## 5. Discussion

[43] The overall accuracy of the blended SWE product is encouraging, benchmarked by its better agreement, compared to SNODAS, with densely sampled in situ observations from six snow survey sites consisting of ~3600 measurements. One major difference between the reconstruction approach and SNODAS is in the usage of observed snow cover information. For SNODAS, observed

SCA is assimilated and used as a mask for model estimates of SWE, but information about snow cover depletion is not ingested into the model. In the reconstruction approach, snow cover depletion information is used by back-integrating snowmelt from zero to maximum snow cover indicated by satellite SCA, which may have contributed to the better quality of blended SWE relative to SNODAS SWE. On a related note, the SCA interpolation approach used here was quite different from *Dozier et al.* [2008]. First, we removed images with poor viewing geometry to reduce the sensitivity of the SCA retrieval to viewing geometry. We then interpolated the SCA images based on cumulative melt flux—an approach not used by *Dozier et al.* [2008]. The benefit of our approach is that we use a dynamically changing and physically relevant variable for interpolation of the SCA images. Application of the reconstruction and blending method to other mountain watersheds depends on the availability and quality of observation sources, as well as better understanding of the error sources.

[44] Mean absolute error of reconstructed SWE is 47% of observed SWE, with percent errors ranging from  $-78.3\%$  to  $18.7\%$  over different snow surveys. The reconstruction error is larger than that of previous applications in much smaller study areas. For example, *Molotch* [2009] found 23% mean absolute error in the application to the Rio Grande headwaters ( $3419 \text{ km}^2$ ) during 2001 and 2002 using Landsat  $f_{SCA}$  images. *Jepsen et al.* [2012] reported reconstruction errors in the range of  $-23\%$  to  $27\%$  for the Tokopah Basin ( $19.1 \text{ km}^2$ ), and  $-37\%$  to  $34\%$  for the Green Lake 4 Valley ( $2.2 \text{ km}^2$ ) during year 1996–2007, both basins with significant areas above treeline.  $R^2$  between reconstructed and observed SWE is 0.74 over 2000–2012, comparing to 0.84 and 0.61 in *Jepsen et al.* [2012] for their two study areas. The spatial point density of evaluation data are comparable between the current and the comparative studies; the evaluation data used in the Tokopah Basin were the same data used by *Jepsen et al.* [2012], and the sampling plan used at the other sites included over 200 measurements per  $\text{km}^2$ , which is very similar to *Molotch* [2009]. Notwithstanding, the six snow survey sites in the current study covers only 0.2% of the model domain. In comparison, snow surveys cover 2.8% of the model domain in *Molotch* [2009], and model domains are aligned with snow survey sites in *Jepsen et al.* [2012]. Besides the density and availability of evaluation data, errors in the reconstruction can likely be attributed to the following error sources: (1) the input surface meteorological and radiative forcing from NLDAS; (2) the downscaling of surface forcing over topographically complex terrains; (3) the  $f_{SCA}$  satellite retrievals, including the failure to discriminate clouds from snow, and interpolation of  $f_{SCA}$  across temporal gaps caused by cloud contamination; (4) the treatment of forest cover; (5) snow albedos calculated by the parameterization scheme that does not account for spatial variability; and (6) significant snow accumulation during some ablation seasons. Based on the sensitivity tests (section 4), downwelling longwave radiation, snow albedo, forest density, and turbulent fluxes are all potentially important areas to be addressed in order to reduce errors and uncertainties in reconstructed SWE. The quality of blended SWE depends on the accuracy of the snow sen-

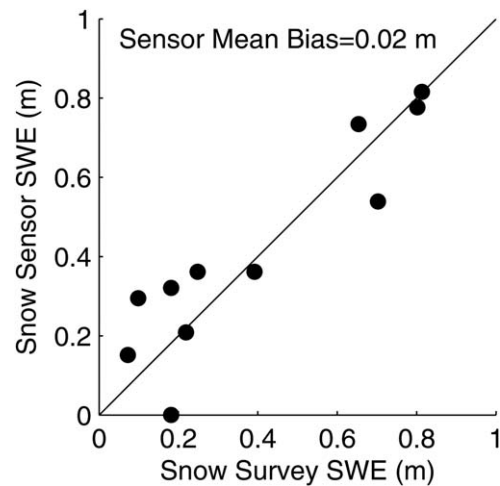


**Figure 14.** Comparison of snow sensor SWE (“point” values at snow sensor site) and mean snow survey SWE over the reconstruction model pixel ( $15 \text{ arc second} \times 15 \text{ arc second}$ , about  $500 \text{ m} \times 500 \text{ m}$ ) surrounding the snow sensor. Comparison over 11 snow surveys near five snow sensor sites (see Figure 1) are shown.

sors as well. A comparison between snow sensor and snow survey SWE suggests that some snow sensors could have a high bias in representing the  $500 \text{ m} \times 500 \text{ m}$  area surrounding a given snow sensor, although the mean bias (hence the impact on blended SWE) could be much smaller (Figure 14). This potentially small mean bias should be distinguished from the expectedly high bias of using mean SWE over snow sensors as an estimate of mean SWE across the Sierra Nevada (Figure 12).

[45] The blended SWE product developed here could help evaluate regional climate models [*Caldwell et al.*, 2009] and land surface/ecosystem models on watershed scales [*Kimball et al.*, 1997; *Pan et al.*, 2003; *Tague et al.*, 2004]. Daily precipitation estimates can be derived from SWE changes, which can be used in diagnosing high-impact weather systems, such as atmospheric rivers [*Guan et al.*, 2010]. Future development of the reconstruction model calls for improved observations and better treatment of the model forcing. For example, downwelling longwave radiation from different algorithms [*Flerchinger et al.*, 2009] need to be assessed. The accuracy of albedo products from MODSCAG needs to be examined. The effects of forest cover and turbulent fluxes need to be better constrained in models. The snow sensor network should better cover the lower and higher elevations and better cover locations with large spatial SWE variability in order to better constrain spatial SWE estimates.

## 6. Conclusions

[46] SWE bias is  $-0.193$ ,  $0.001$ , and  $-0.181 \text{ m}$ , respectively, in mean reconstructed, blended, and SNODAS SWE, averaged over 17 snow surveys from six survey sites in the Sierra Nevada. Corresponding mean RMS errors are  $0.252$ ,  $0.205$ , and  $0.254 \text{ m}$ , respectively. The overall accuracy of blended SWE is higher than SNODAS SWE based on validation against snow survey observations. Mean

snow sensor SWE is best represented in blended SWE, with negligible difference from the snow sensor observation. On average, full natural flow correlates better with reconstructed SWE than with snow sensor and SNODAS SWE over the 19 watersheds, particularly in parts of the Sierra Nevada critical for the California State Water Project. Correlations are better with blended SWE than with snow sensor and SNODAS SWE over the majority of the watersheds in the late season when point-based streamflow predictions are problematic. Sensitivity tests indicate that large errors and uncertainties in reconstructed SWE are associated with downwelling longwave radiation, snow albedo, forest density, and turbulent fluxes. Domain-mean blended SWE is relatively insensitive to the number of snow sensors used for blending, but local sensitivities of above 0.1 m exist, especially when only 25% of the sensors are retained. Continued observational and modeling efforts are needed to reduce uncertainties in SWE estimates across large, hydrologically important watersheds, and to improve water resource management in these areas.

[47] **Acknowledgments.** This research was supported by NASA grants NNX08AH18G, NNX11AK35A, NNX11AK35G, and NNX10AO97G, NSF grants EAR 1032295 and EAR 1141764, USDA grant 2012-67003-19802, the NOAA RISA Western Water Assessment, and United States American Recovery and Reinvestment Act funds. Gridded snow survey data from five sites are provided by L. Meromy, S. Roberts, and J. Sickman. L. Lestak provided technical support. D.E.W.'s and B.G.'s contributions, and part of N.P.M.'s, S.M.J.'s and T.H.P.'s contributions, to this study were carried out on behalf of the Jet Propulsion Laboratory, California Institute of Technology, under a contract with the National Aeronautics and Space Administration.

## References

- Alpert, P. (1986), Mesoscale indexing of the distribution of the orographic precipitation over high mountains, *J. Clim. Appl. Meteorol.*, *25*, 532–545, doi:10.1175/1520-0450(1986)025<0532:MIOTDO>2.0.CO;2.
- Andreadis, K. M., and D. P. Lettenmaier (2006), Assimilating remotely sensed snow observations into a macroscale hydrology model, *Adv. Water Resour.*, *29*, 872–886, doi:10.1016/j.advwatres.2005.08.004.
- Bales, R. C., N. P. Molotch, T. H. Painter, M. D. Dettinger, R. Rice, and J. Dozier (2006), Mountain hydrology of the western United States, *Water Resour. Res.*, *42*, W08432, doi:10.1029/2005WR004387.
- Barrett, A. P. (2003), National Operational Hydrologic Remote Sensing Center SNOw Data Assimilation System (SNODAS) products at NSIDC, Spec. Rep. 11, Natl. Snow and Ice Data Cent., Coop. Inst. for Res. in Environ. Sci., Univ. of Colo., Boulder, Colo., USA.
- Barros, A. P., and D. P. Lettenmaier (1994), Dynamic modeling of orographically induced precipitation, *Rev. Geophys.*, *32*, 265–284, doi:10.1029/94RG00625.
- Brubaker, K., A., Rango, and W., Kustas (1996), Incorporating radiation inputs into the snowmelt runoff model, *Hydrol. Processes*, *10*, 1329–1343, doi:10.1002/(SICI)1099-1085(199610)10:10<1329::AID-HYP464>3.0.CO;2-W.
- Caldwell, P., H.-N. S. Chin, D. C. Bader, and G. Bala (2009), Evaluation of a WRF dynamical downscaling simulation over California, *Clim. Change*, *95*, 499–521, doi:10.1007/s10584-009-9583-5.
- Carroll, S. S., and Cressie, N. (1996), A comparison of geostatistical methodologies used to estimate snow water equivalent, *J. Am. Water Resour. Assoc.*, *32*, 267–278, doi:10.1111/j.1752-1688.1996.tb03450.x.
- Carroll, T., D. Cline, G. Fall, A. Nilsson, L. Li, and A. Rost (2001), NOHRSC operations and the simulation of snow cover properties for the coterminous U.S., *Proc. Western Snow Conf.*, *69*, 1–14.
- Christensen, N. S., A. W. Wood, N. Voisin, D. P. Lettenmaier, and R. N. Palmer (2004), The effects of climate change on the hydrology and water resources of the Colorado River Basin, *Clim. Change*, *62*, 337–363, doi:10.1023/B:CLIM.0000013684.13621.1f.
- Cline, D. W., and T. R. Carroll (1999), Inference of snow cover beneath obscuring clouds using optical remote sensing and a distributed snow energy and mass balance model, *J. Geophys. Res.*, *104*, 19,631–19,644, doi:10.1029/1999JD900249.
- Cline, D. W., R. C. Bales, and J. Dozier (1998), Estimating the spatial distribution of snow in mountain basins using remote sensing and energy balance modeling, *Water Resour. Res.*, *34*, 1275–1285, doi:10.1029/97WR03755.
- Déry, S. J., V. V. Salomonson, M. Stieglitz, D. K. Hall, and I. Appel (2005), An approach to using snow areal depletion curves inferred from MODIS and its application to land surface modelling in Alaska, *Hydrol. Processes*, *19*, 2755–2774, doi:10.1002/hyp.5784.
- Dozier, J. (1980), A clear-sky spectral solar radiation model for snow-covered mountainous terrain, *Water Resour. Res.*, *16*, 709–718, doi:10.1029/WR016i004p00709.
- Dozier, J. (2011), Mountain hydrology, snow color, and the fourth paradigm, *Eos Trans. AGU*, *92*, 373–375, doi:10.1029/2011EO430001.
- Dozier, J., and J. Frew (1990), Rapid calculation of terrain parameters for radiation modeling from digital elevation data, *IEEE Trans. Geosci. Remote Sens.*, *28*, 963–969, doi:10.1109/36.58986.
- Dozier, J., and T. H. Painter (2004), Multispectral and hyperspectral remote sensing of alpine snow properties, *Annu. Rev. Earth Planet. Sci.*, *32*, 465–494, doi:10.1146/annurev.earth.32.101802.120404.
- Dozier, J., T. H. Painter, K. Rittger, and J. E. Frew (2008), Time-space continuity of daily maps of fractional snow cover and albedo from MODIS, *Adv. Water Resour.*, *31*, 1515–1526, doi:10.1016/j.advwatres.2008.08.011.
- Durand, M., N. P. Molotch, and S. A. Margulis (2008), A Bayesian approach to snow water equivalent reconstruction, *J. Geophys. Res.*, *113*, D20117, doi:10.1029/2008JD009894.
- Elder, K., J. Dozier, and J. Michaelsen (1991), Snow accumulation and distribution in an alpine watershed, *Water Resour. Res.*, *27*, 1541–1552, doi:10.1029/91WR00506.
- Erickson, T. A., M. W. Williams, and A. Winstral (2005), Persistence of topographic controls on the spatial distribution of snow in rugged mountain terrain, Colorado, United States, *Water Resour. Res.*, *41*, W04014, doi:10.1029/2003WR002973.
- Erxleben, J., K. Elder, and R. Davis (2002), Comparison of spatial interpolation methods for estimating snow distribution in the Colorado Rocky Mountains, *Hydrol. Processes*, *16*, 3627–3649, doi:10.1002/hyp.1239.
- Farr, T. G., et al. (2007), The shuttle radar topography mission, *Rev. Geophys.*, *45*, RG2004, doi:10.1029/2005RG000183.
- Fassnacht, S. R., K. A. Dressler, and R. C. Bales (2003), Snow water equivalent interpolation for the Colorado River Basin from snow telemetry (SNOTEL) data, *Water Resour. Res.*, *39*(8), 1208, doi:10.1029/2002WR001512.
- Flerchinger, G. N., W. Xaio, D. Marks, T. J. Sauer, and Q. Yu (2009), Comparison of algorithms for incoming atmospheric long-wave radiation, *Water Resour. Res.*, *45*, W03423, doi:10.1029/2008WR007394.
- Guan, B., N. P. Molotch, D. E. Waliser, E. J. Fetzer, and P. J. Neiman (2010), Extreme snowfall events linked to atmospheric rivers and surface air temperature via satellite measurements, *Geophys. Res. Lett.*, *37*, L20401, doi:10.1029/2010GL044696.
- Haddeland, I., et al. (2011), Multimodel estimate of the global terrestrial water balance: Setup and first results, *J. Hydrometeorol.*, *12*, 869–884, doi:10.1175/2011JHM1324.1.
- Hodges, D. B., et al. (1983), Final tactical decision aid (FTDA) for infrared (8–12 micron) systems—Technical background, Sci. Rep. 5, Air Force Geophys. Lab., Hanscom AFB, Bedford, Mass.
- Idso, S. B. (1981), A set of equations for full spectrum and 8- to 14- $\mu$ m and 10.5- to 12.5- $\mu$ m thermal radiation from cloudless skies, *Water Resour. Res.*, *17*, 295–304, doi:10.1029/WR017i002p00295.
- Jepsen, S. M., N. P. Molotch, M. W. Williams, K. E. Rittger, and J. O. Sickman (2012), Interannual variability of snowmelt in the Sierra Nevada and Rocky Mountains, USA: Examples from two alpine watersheds, *Water Resour. Res.*, *48*, W02529, doi:10.1029/2011WR011006.
- Jin, J., X. Gao, S. Sorooshian, Z. L. Yang, R. C. Bales, R. E. Dickinson, S. F. Sun, and G. X. Wu (1999), One-dimensional snow water and energy balance model for vegetated surfaces, *Hydrol. Processes*, *13*, 2467–2482, doi:10.1002/(SICI)1099-1085(199910)13:14/15<2467::AID-HYP861>3.0.CO;2-J.
- Jordan, R. (1991), A one-dimensional temperature model for a snow cover: Technical documentation for SNTherm.89, Spec. Rep. 91-16, 49 pp., U.S. Army Cold Reg. Res. and Eng. Lab., Hanover, N. H.
- Kimball, J. S., M. A. White, and S. W. Running (1997), BIOME-BGC simulations of stand hydrologic processes for BOREAS, *J. Geophys. Res.*, *102*, 29,043–29,051, doi:10.1029/97JD02235.

- Kotchenova, S. Y., and E. F. Vermote (2007), Validation of a vector version of the 6S radiative transfer code for atmospheric correction of satellite data, Part II: Homogeneous Lambertian and anisotropic surfaces, *Appl. Opt.*, *46*, 4455–4464, doi:10.1364/AO.46.004455.
- Kotchenova, S. Y., E. F. Vermote, R. Matarrese, and F. J. Klemm, Jr. (2006), Validation of a vector version of the 6S radiative transfer code for atmospheric correction of satellite data, Part I: Path radiance, *Appl. Opt.*, *45*, 6762–6774, doi:10.1364/AO.45.006762.
- Kumar, M., D. Marks, J. Dozier, M. Reba, and A. Winstral (2013), Evaluation of distributed hydrologic impacts of temperature-index and energy-based snow models, *Adv. Water Resour.*, *56*, 77–89, doi:10.1016/j.advwatres.2013.03.006.
- Lowry, C. S., J. S. Deems, S. P. Loheide II, and J. D. Lundquist (2010), Linking snowmelt-derived fluxes and groundwater flow in a high elevation meadow system, Sierra Nevada Mountains, *California. Hydrol. Processes*, *24*, 2821–2833, doi:10.1002/hyp.7714.
- Liston, G. E., O. Bruland, H. Elvehøy, and K. Sand (1999), Below-surface ice melt on the coastal Antarctic ice sheet, *J. Glaciol.*, *45*, 273–285, doi:10.3189/002214399793377130.
- Luzio, M. D., Johnson G. L., Daly C., Eischeid J. K., and Arnold J. G. (2008), Constructing retrospective gridded daily precipitation and temperature datasets for the conterminous United States, *J. Appl. Meteorol. Climatol.*, *47*, 475–497, doi:10.1175/2007JAMC1356.1.
- Martinez, J., and A. Rango (1981), Areal distribution of snow water equivalent evaluated by snow cover monitoring, *Water Resour. Res.*, *17*, 1480–1488, doi:10.1029/WR017i005p01480.
- Maurer, E. P. (2007), Uncertainty in hydrologic impacts of climate change in the Sierra Nevada, California, under two emissions scenarios, *Clim. Change*, *82*, 309–325, doi:10.1007/s10584-006-9180-9.
- Meromy, L., N. P. Molotch, T. E. Link, S. R. Fassnacht, and R. Rice (2012), Subgrid variability of snow water equivalent at operational snow stations in the western USA, *Hydrol. Processes*, doi:10.1002/hyp.9355.
- Molotch, N. P. (2009), Reconstructing snow water equivalent in the Rio Grande headwaters using remotely sensed snow cover data and a spatially distributed snowmelt model, *Hydrol. Processes*, *23*, 1076–1089, doi:10.1002/hyp.7206.
- Molotch, N. P., and R. C. Bales (2005), Scaling snow observations from the point to the grid element: Implications for observation network design, *Water Resour. Res.*, *41*, W11421, doi:10.1029/2005WR004229.
- Molotch, N. P., and R. C. Bales (2006), SNOTEL representativeness in the Rio Grande headwaters on the basis of physiographics and remotely sensed snow cover persistence, *Hydrol. Processes*, *20*, 723–739, doi:10.1002/hyp.6128.
- Molotch, N. P., and S. A. Margulis (2008), Estimating the distribution of snow water equivalent using remotely sensed snow cover data and a spatially distributed snowmelt model: A multi-resolution, multi-sensor comparison, *Adv. Water Resour.*, *31*, 1503–1514, doi:10.1016/j.advwatres.2008.07.017.
- Molotch, N. P., S. A. Margulis, and S. M. Jepsen (2010), Response to comment by A.G. Slater, M.P. Clark, and A.P. Barrett on ‘Estimating the distribution of snow water equivalent using remotely sensed snow cover data and a spatially distributed snowmelt model: A multi-resolution, multi-sensor comparison’. *Adv. Water Resour.*, *33*, 231–239, doi:10.1016/j.advwatres.2009.11.008.
- Molotch, N. P., S. R. Fassnacht, R. C. Bales, and S. R. Helfrich (2004), Estimating the distribution of snow water equivalent and snow extent beneath cloud cover in the Salt-Verde River basin, Arizona, *Hydrol. Processes*, *18*, 1595–1611, doi:10.1002/hyp.1408.
- Molotch, N. P., M. T. Colee, R. C. Bales, J. Dozier (2005a), Estimating the spatial distribution of snow water equivalent in an alpine basin using binary regression tree models: The impact of digital elevation data and independent variable selection, *Hydrol. Processes*, *19*, 1459–1479, doi:10.1002/hyp.5586.
- Molotch, N. P., R. C. Bales, M. T. Colee, and J. Dozier (2005b), Estimating the spatial distribution of snow water equivalent in an alpine basin using binary regression tree models: The impact of digital elevation data and independent variable selection, *Hydrol. Processes*, *19*, 1459–1479, doi:10.1002/hyp.5586.
- Neiman, P. J., F. M. Ralph, G. A. Wick, J. D. Lundquist, and M. D. Dettinger (2008), Meteorological characteristics and overland precipitation impacts of atmospheric rivers affecting the West Coast of North America based on eight years of SSM/I satellite observations, *J. Hydrometeorol.*, *9*, 22–47, doi:10.1175/2007JHM855.1.
- Newald, T. G., and M. Lehning (2011), Altitudinal dependency of snow amounts in two small alpine catchments: Can catchment wide snow amounts be estimated via single snow or precipitation stations?, *Ann. Glaciol.*, *52*, 153–158, doi:10.3189/172756411797252248.
- Niu, G.-Y., K.-W. Seo, Z.-L. Yang, C. Wilson, H. Su, J. Chen, and M. Rodell (2007), Retrieving snow mass from GRACE terrestrial water storage change with a land surface model, *Geophys. Res. Lett.*, *34*, L15704, doi:10.1029/2007GL030413.
- Painter, T. H., K. Rittger, C. McKenzie, P. Slaughter, R. E. Davis, and J. Dozier (2009), Retrieval of subpixel snow-covered area, grain size, and albedo from MODIS, *Remote Sens. Environ.*, *113*, 868–879, doi:10.1016/j.rse.2009.01.001.
- Pan, M., et al. (2003), Snow process modeling in the North American Land Data Assimilation System (NLDAS): 2. Evaluation of model simulated snow water equivalent, *J. Geophys. Res.*, *108*(D22), 8850, doi:10.1029/2003JD003994.
- Pandey, G. R., D. R. Cayan, and K. P. Georgakakos (1999), Precipitation structure in the Sierra Nevada of California during winter, *J. Geophys. Res.*, *104*, 12,019–12,030, doi:10.1029/1999JD900103.
- Peck, E. L., V. C. Bissell, E. B. Jones, and D. L. Burge (1971), Evaluation of snow water equivalent by airborne measurement of passive terrestrial gamma radiation, *Water Resour. Res.*, *7*, 1151–1159, doi:10.1029/WR007i005p01151.
- Raleigh, M. S., and J. D. Lundquist (2012), Comparing and combining SWE estimates from the SNOW-17 model using PRISM and SWE reconstruction, *Water Resour. Res.*, *48*, W01506, doi:10.1029/2011WR010542.
- Raleigh, M. S., K. Rittger, C. E. Moore, B. Henn, J. A. Lutz, and J. D. Lundquist (2013), Ground-based testing of MODIS fractional snow cover in subalpine meadows and forests of the Sierra Nevada, *Remote Sens. Environ.*, *128*, 44–57, doi:10.1016/j.rse.2012.09.016.
- Rice, R., R. C. Bales, T. H. Painter, and J. Dozier (2011), Snow water equivalent along elevation gradients in the Merced and Tuolumne River basins of the Sierra Nevada, *Water Resour. Res.*, *47*, W08515, doi:10.1029/2010WR009278.
- Rittger, K. E. (2012), Spatial estimates of snow water equivalent in the Sierra Nevada, Ph.D. thesis, Univ. of Calif., Santa Barbara, Calif.
- Rittger, K., T. H. Painter, and J. Dozier (2013), Assessment of methods for mapping snow cover from MODIS, *Adv. Water Resour.*, *51*, 367–380, doi:10.1016/j.advwatres.2012.03.002.
- Rutter, N., D. Cline, and L. Li (2008), Evaluation of the NOHRSC snow model (NSM) in a one-dimensional mode, *J. Hydrometeorol.*, *9*, 695–711, doi:10.1175/2008JHM861.1.
- Shi, J. (2008), Active microwave remote sensing systems and applications to snow monitoring, in *Advances in Land Remote Sensing: System, Modeling, Inversion and Application*, edited by S. Liang, pp. 19–49, Springer, Berlin.
- Slater, A. G., A. P. Barrett, M. P. Clark, J. D. Lundquist, and M. S. Raleigh (2012), Uncertainty in seasonal snow reconstruction: Relative impacts of model forcing and image availability, *Adv. Water Resour.*, *55*, 165–177, doi:10.1016/j.advwatres.2012.07.006.
- Sturm, M., and A. M. Wagner (2010), Using repeated patterns in snow distribution modeling: An Arctic example, *Water Resour. Res.*, *46*, W12549, doi:10.1029/2010WR009434.
- Syed, T. H., J. S. Famiglietti, and D. P. Chambers (2009), GRACE-based estimates of terrestrial freshwater discharge from basin to continental scales, *J. Hydrometeorol.*, *10*, 22–40, doi:10.1175/2008JHM993.1.
- Tague, C. L., C. McMichael, A. Hope, J. Choate, and R. Clark (2004), Application of the RHESys model to a California semiarid shrubland watershed, *J. Am. Water Resour. Assoc.*, *40*, 575–589, doi:10.1111/j.1752-1688.2004.tb04444.x.
- US Army Corps of Engineers (1956), *Snow hydrology: Summary report of the snow investigations*, 462 pp., North Pac. Div., Portland, Oreg.
- VanShaar, J. R., I. Haddeland, and D. P. Lettenmaier (2002), Effects of land-cover changes on the hydrological response of interior Columbia River basin forested catchments, *Hydrol. Processes*, *16*, 2499–2520, doi:10.1002/hyp.1017.
- Warren, S. G., and W. J. Wiscombe (1980), A model for the spectral albedo of snow, II, Snow containing atmospheric aerosols, *J. Atmos. Sci.*, *37*, 2734–2745, doi:10.1175/1520-0469(1980)037<2734:AMFTSA>2.0.CO;2.
- Welch, S. C., B. Kerkez, R. C. Bales, S. D. Glaser, K. Rittger, and R. R. Rice (2013), Sensor placement strategies for snow water equivalent (SWE) estimation in the American River basin, *Water Resour. Res.*, *49*, 891–903, doi:10.1002/wrcr.20100.
- Winstral, A., K. Elder, and R. E. Davis (2002), Spatial snow modeling of wind-redistributed snow using terrain-based parameters, *J. Hydrometeorol.*, *3*, 524–538, doi:10.1175/1525-7541(2002)003<0524:SSMOWR>2.0.CO;2.